

Robotic Contact Juggling

J. Zachary Woodruff, (*Member, IEEE*), and Kevin M. Lynch, (*Fellow, IEEE*)

Abstract—We define “robotic contact juggling” to be the purposeful control of the motion of a three-dimensional smooth object as it rolls freely on a motion-controlled robot manipulator, or “hand.” While specific examples of robotic contact juggling have been studied before, in this paper we provide the first general formulation and solution method for the case of an arbitrary smooth object in single-point rolling contact on an arbitrary smooth hand. Our formulation splits the problem into four subproblems: (1) deriving the second-order rolling kinematics; (2) deriving the three-dimensional rolling dynamics; (3) planning rolling motions that satisfy the rolling dynamics; and (4) feedback stabilization of planned rolling trajectories. The theoretical results are demonstrated in simulation and experiment using feedback from a high-speed vision system.

I. INTRODUCTION

CONTACT juggling is a form of object manipulation where the juggler controls the motion of an object, often a crystal ball, as it rolls on the juggler’s arms, hands, torso, or even shaved head. The manipulation is nonprehensile (no form- or force-closure grasp) and dynamic, i.e., momentum plays a crucial role. An example is shown in Figure 1. This is a variation of a contact juggling skill called “the butterfly,” and robotic implementations of the butterfly have been described in [1]–[3]. The object (typically a ball) is initially at rest on the palm, and the goal state is rest on the back of the hand. The hand is accelerated to cause the object to roll up and over the fingers to the other side of the hand.

We define “robotic contact juggling” to be the purposeful control of the motion of a three-dimensional smooth object as it rolls freely on a motion-controlled robot manipulator, or “hand.” Specific examples of robotic contact juggling have been studied before, such as the butterfly example mentioned above and specific geometries such as a sphere rolling on a motion-controlled flat plate. This paper extends previous work by providing the first general formulation and solution method for the case of an arbitrary smooth object in single-point rolling contact on an arbitrary smooth hand. Our formulation splits the problem into four subproblems: (1) deriving the second-order rolling kinematics; (2) deriving the three-dimensional rolling dynamics; (3) planning rolling motions that satisfy the rolling dynamics and achieve the desired goal state; and (4) feedback stabilization of planned rolling trajectories. The theoretical results are demonstrated in

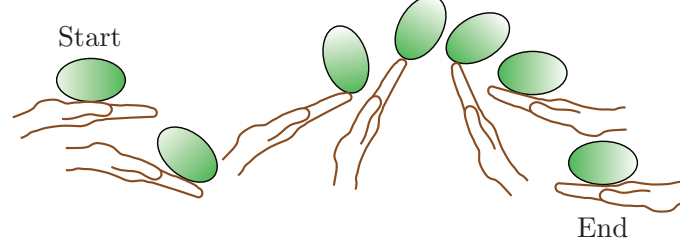


Fig. 1. Example of a contact juggling skill known as “the butterfly.” A smooth object is initially at rest in the palm of the hand, and the motion of the hand causes the object to roll to the back of the hand.

simulation and experiment using feedback from a high-speed vision system.

A. Background

When a three-dimensional rigid body (the object) is in single-point contact with another rigid body (the hand), the configuration of the object relative to the hand is five dimensional: the six degrees of freedom of the object subject to the single constraint that the distance to the hand is zero. This five-dimensional configuration space can be parameterized by two coordinates $\mathbf{u}_o = (u_o, v_o)$ describing the contact location on the surface of the object, two coordinates $\mathbf{u}_h = (u_h, v_h)$ describing the contact location on the surface of the hand, and one coordinate ψ describing the angle of “spin” between frames fixed to each body at the contact point. Collectively the contact configuration is written $\mathbf{q} = (u_o, v_o, u_h, v_h, \psi)$ (Figure 2).

Rolling contact is maintained when there is no relative linear velocity at the contact $\mathbf{v}_{\text{rel}} = (v_x, v_y, v_z) = \mathbf{0}$ (i.e. no slipping or separation). For rolling bodies modeled with a point contact, no torques are transmitted through the contact, and relative spin about the contact normal is allowed. We refer to this as “rolling.” For rolling bodies modeled with a soft contact, torques can be transmitted and no relative spin about the contact normal is allowed ($\omega_{\text{rel},z} = \omega_z = 0$). We refer to this as “pure rolling” (or “soft rolling”).

B. Paper Outline

As mentioned above, our approach to contact juggling divides the problem into four subproblems: (1) deriving the second-order rolling kinematics; (2) deriving the rolling dynamics; (3) planning rolling motions that satisfy the dynamics; and (4) feedback stabilization of rolling trajectories. An outline of each subproblem is given below.

This work supported in part by the NSF Graduate Research Fellowship Program under Grant DGE-1324585, and in part by the NSF under Grant IIS-1527921.

J. Z. Woodruff (jzwoodruff@u.northwestern.edu, corresponding author) and K. M. Lynch (kmlynch@northwestern.edu) are with the Center for Robotics and Biosystems (CRB), Northwestern University, Evanston, IL 60208 USA. K. M. Lynch is also affiliated with the Northwestern Institute on Complex Systems, Evanston, IL 60201 USA.

Open source code that accompanies this paper can be found at: https://github.com/zackwoodruff/rolling_dynamics

Taylor and Rodriguez perform shape optimization of manipulators and motion planning for dynamic planar manipulation tasks [12]. Ryu and Lynch derive a feedback controller that enables a planar, disk-shaped manipulator to balance a disk while tracking trajectories [13]. Erumalla et al. perform throwing, catching, and balancing for an experimental setup of a disk on a disk-shaped manipulator [14]. Lippiello et al. develop a control framework for nonprehensile planar rolling dynamic manipulation and validate it experimentally for a disk on a rotating disk [15]. Serra et al. [16] apply a passivity-based approach to the same problem.

2) *General Spatial Rolling*: General methods exist for simulating rigid bodies in contact, some of which explicitly handle rolling contacts. Anitescu et al. develop a general method for contact dynamic simulations [17]. It uses a complementary formulation that allows simulation of multiple rigid bodies, and uses the first-order-rolling equations from Montana [6] to solve for contact constraints. Liu and Wang develop a time-stepping method for rigid-body dynamics that specifically addresses rolling contacts [18]. Duindam et al. model the kinematics and dynamics of compliant contact between bodies moving in Euclidean space [19]. There are many software packages for performing dynamic simulations [20], and a subset of those can explicitly handle rolling constraints. Because each object state is represented as an independent six-dof rigid body, these methods allow for non-zero contact distances (separation or penetration) and are not specifically focused on modeling the rolling interaction between objects.

3) *Prehensile Spatial Rolling*: There are many works that address prehensile motion planning for a ball (sphere) that is in contact with a stationary plate and actuated by a second, opposing, plate [21]–[25]. Sarkar et al. expand the second-order kinematics equations to generate a dynamic model for an object caged between two surfaces [8]. They use feedback linearization to control dynamic rolling motions for two planes in contact with a sphere.

4) *Nonprehensile Spatial Rolling*: Jia and Erdmann derive dynamic equations and show the observability of an object with an orthogonal parameterization on a flat plate equipped with a contact position sensor [26]. Choudhury and Lynch stabilize the orientation of a ball rolling in an ellipsoidal dish actuated along a single degree of freedom [27]. Both these works assume no rotational motion of the hand which simplifies the modeling and control problem.

Gahleitner models a sphere with three rotation inputs balancing another sphere, designs a stabilizing controller, and validates the results experimentally [28]. Additionally there are numerous papers on control of an object in nonprehensile contact with a plate that control the contact location on the hand but do not consider the orientation of the object [29], [30]. To our knowledge, only one paper studies dynamic, nonprehensile planning for a ball on a plate while considering the full position and pose of the ball [31]. Works by Milne (part III.XV of [32]) and Weltner [33] derive analytical solutions for a sphere rolling on a rotating plate with a constant angular velocity, and we use these solutions to validate our rolling simulation in Section V.

As mentioned in Section I-C, to our knowledge this paper

is the first to formulate the rolling dynamics of a rigid body rolling on a six-DoF motion-controlled manipulator for general manipulator and object shapes.

III. NOTATION

For general variables, matrices and vectors are bold uppercase (e.g., \mathbf{R}) and bold lowercase (e.g., \mathbf{r}) letters, respectively. Scalars are non-bold italic (e.g., u), and coordinate frames are expressed as lowercase letters in curly brackets (e.g., $\{s\}$). Notations for variables and operators (mappings between spaces) are shown in Table I, and selected operator expressions are given in Appendix A.

The space frame (i.e., inertial reference) is defined as $\{s\}$, and the hand frame is define as $\{h\}$. The object frame $\{o\}$ is located at its center of mass and aligned with the principal axes. Four frames with coincident origins, $\{p_i\}$ and $\{c_i\}$ ($i \in \{o, h\}$) are defined at the current object-hand contact, where $\{p_i\}$ is fixed relative to the body frame $\{i\}$ and $\{c_i\}$ is fixed in $\{s\}$ (see Figure 2).

Double subscripts indicate a comparison between two frames expressed in the frame of the first subscript. For example, \mathbf{R}_{so} gives the rotation matrix relating frame $\{o\}$ relative to frame $\{s\}$ expressed in $\{s\}$, and \mathcal{V}_{sh} gives the twist of the hand relative to the space frame $\{s\}$ expressed in $\{s\}$. In deriving the kinematics and dynamics equations, we often compare the relative velocities between different frames expressed in a third frame which we denote with a preceding superscript. For example, ${}^{c_h}\mathcal{V}_{p_h p_o}$ gives the twist of frame $\{p_o\}$ relative to $\{p_h\}$ expressed in the $\{c_h\}$ frame and is equivalent to $[\text{Ad}_{\mathbf{T}_{c_h s}}](\mathcal{V}_{sp_o} - \mathcal{V}_{sp_h})$, where $[\text{Ad}_{\mathbf{T}_{ab}}]$ is the 6×6 adjoint map matrix associated with $\mathbf{T}_{ab} \in SE(3)$, the transformation matrix representing the frame $\{b\}$ relative to frame $\{a\}$. “Body twists” are defined as ${}^i\mathcal{V}_{si}$, and represent the twists of the body relative to the space frame, expressed in its own coordinate frame $\{i\}$. Variables must be expressed in the same frame to compare, and we resolve the kinematics and dynamics expressions in the contact frame of the hand $\{c_h\}$.

The surface of each body is represented by an orthogonal parameterization: $\mathbb{F}_i : \mathbf{u}_i \rightarrow \mathbb{R}^3 : (u_i, v_i) \mapsto (x_i, y_i, z_i)$, where the coordinates (x_i, y_i, z_i) are expressed in the $\{i\}$ frame. We assume that \mathbb{F}_i is continuous up to the third derivative (class C^3), so that the local contact geometry (contact frames associated with the first derivative of \mathbb{F}_i , curvature associated with the second derivative, and derivative of the curvature associated with the third derivative) are uniquely defined. Standard expressions for the local geometry of smooth bodies are given in Appendix B-A.

IV. ROLLING KINEMATICS

A. First-Order Rolling Kinematics

The contact configuration of two bodies in rolling contact can be parameterized by $\mathbf{q} = (u_o, v_o, u_h, v_h, \psi)$ (see Figure 2). First-order kinematics models the evolution of contact coordinates between two rigid bodies when the relative contact velocities are known. The relative twist at the contact in

TABLE I
NOTATION

Variable	Description	Dimensions
$\{\cdot\}$	Coordinate frame	-
\mathbf{r}	Position vector $\mathbf{r} = (x, y, z)$	3×1
Φ	\mathbf{xyz} Euler angles $\Phi = (\theta, \beta, \gamma)$	3×1
\mathbf{R}	Rotation matrix $\mathbf{R} \in SO(3)$	3×3
\mathbf{T}	Transformation matrix $\mathbf{T} \in SE(3)$	4×4
ω	Rotational velocity $\omega = (\omega_x, \omega_y, \omega_z)$	3×1
\mathbf{v}	Linear velocity $\mathbf{v} = (v_x, v_y, v_z)$	3×1
\mathcal{V}	Twist $\mathcal{V} = (\omega, \mathbf{v})$	6×1
α	Rotational accel $\alpha = \dot{\omega} = (\alpha_x, \alpha_y, \alpha_z)$	3×1
\mathbf{a}	Linear accel $\mathbf{a} = \dot{\mathbf{v}} = (a_x, a_y, a_z)$	3×1
$\dot{\mathcal{V}}$	Change in twist $\dot{\mathcal{V}} = (\alpha, \mathbf{a})$	6×1
\mathbf{q}	Contact coords $\mathbf{q} = (u_o, v_o, u_h, v_h, \psi)$	5×1
\mathcal{G}	Spatial inertia matrix	6×6
\mathcal{F}	Wrench $\mathcal{F} = (\tau_x, \tau_y, \tau_z, f_x, f_y, f_z)$	6×1
\mathbf{s}	Dynamic rolling states	22×1
ξ	State and control pair $(\mathbf{s}, {}^h\dot{\mathcal{V}}_{sh})$	28×1
Operator	Description (expressions in Appendix A)	Mapping
$[\cdot]$	Vector to skew-symmetric form	$\mathbb{R}^3 \mapsto so(3)$
$[\text{Ad}_{\mathbf{T}}]$	Adjoint map associated with \mathbf{T}	$SE(3) \mapsto \mathbb{R}^{6 \times 6}$
$[\text{ad}_{\mathcal{V}}]$	Lie bracket matrix form of \mathcal{V}	$\mathbb{R}^6 \mapsto \mathbb{R}^{6 \times 6}$
$\mathbb{F}(\mathbf{u})$	Surface parameterization	$(u, v) \mapsto (x, y, z)$

$\{c_h\}$ is given by ${}^{c_h}\mathcal{V}_{p_h p_o} = \mathcal{V}_{\text{rel}} = [\omega_x \ \omega_y \ \omega_z \ v_x \ v_y \ v_z]^T$. To maintain contact, the non-separation constraint $v_z = 0$ must be satisfied. Enforcing the constraints $v_x = v_y = 0$ ensures rolling without linear slip in the contact tangent plane (rolling). Further, enforcing the constraint $\omega_z = 0$ ensures no relative spinning about the contact normal (pure rolling). We refer to these as the first-order rolling and first-order pure-rolling constraints respectively. The first-order rolling kinematics ($v_x = v_y = v_z = 0$) from [4] can be expressed in matrix form as:

$$\dot{\mathbf{q}} = \mathbf{K}_1(\mathbf{q})\omega_{\text{rel}}, \quad (1)$$

where $\omega_{\text{rel}} = {}^{c_h}\omega_{p_h p_o} = [\omega_x \ \omega_y \ \omega_z]^T$ is the relative rotational velocity at the contact expressed in $\{c_h\}$. The matrix $\mathbf{K}_1(\mathbf{q})$, given in Appendix B-B, maps the relative rotational velocity at the contact to the change in contact coordinates $\dot{\mathbf{q}}$. The dimension of valid contact velocities for rolling and pure rolling are three and two respectively, so the five-dimensional $\dot{\mathbf{q}}$ is subject to constraints given at the end of Appendix B-B.

An expression for the body twist of the object given the body twist of the hand ${}^h\mathcal{V}_{sh}$ and the relative twist at the contact \mathcal{V}_{rel} is used in the dynamics derivation in Section V. The equation is defined as:

$${}^o\mathcal{V}_{so} = [\text{Ad}_{\mathbf{T}_{oh}}]{}^h\mathcal{V}_{sh} + [\text{Ad}_{\mathbf{T}_{och}}]\mathcal{V}_{\text{rel}}, \quad (2)$$

where $\mathcal{V}_{\text{rel}} = {}^{c_h}\mathcal{V}_{p_h p_o}$.

B. Second-Order Rolling Kinematics

The general form of the second-order kinematics gives $\ddot{\mathbf{q}}$ as a function of the current state and $\dot{\mathcal{V}}_{\text{rel}} = {}^{c_h}\dot{\mathcal{V}}_{p_h p_o} = [\alpha_x \ \alpha_y \ \alpha_z \ a_x \ a_y \ a_z]^T$ (the derivative of the relative twist at the contact expressed in $\{c_h\}$). This expression includes the relative rotational accelerations $\alpha_{\text{rel}} = [\alpha_x \ \alpha_y \ \alpha_z]^T$ and the

relative linear accelerations $\mathbf{a}_{\text{rel}} = [a_x \ a_y \ a_z]^T$. The second-order kinematics from [4] can be expressed in matrix form as:

$$\ddot{\mathbf{q}} = \mathbf{K}_2(\mathbf{q}, \omega_{\text{rel}}) + \mathbf{K}_3(\mathbf{q})\dot{\mathcal{V}}_{\text{rel}}, \quad (3)$$

where the terms $\mathbf{K}_2(\mathbf{q}, \omega_{\text{rel}})$ and $\mathbf{K}_3(\mathbf{q})$ are given in Appendix B-C.

This general form allows relative sliding at the contact. To maintain rolling, $\dot{\mathcal{V}}_{\text{rel}}$ must lie in a three-dimensional subspace satisfying

$$\mathbf{a}_{\text{rel}} = \mathbf{a}_{\text{roll}} = [a_x \ a_y \ a_z]_{\text{roll}}^T = -\omega_{\text{rel}} \times {}^{c_h}\mathbf{v}_{c_o o}, \quad (4)$$

as derived in Eq. (60) of [4]. To maintain pure rolling, $\dot{\mathcal{V}}_{\text{rel}}$ must lie in a two-dimensional subspace additionally satisfying the constraint $\alpha_z = \alpha_{z, \text{pr}}$, which is different from the result found in [4], and is derived in Appendix B-C1. For the case of pure rolling $\omega_z = 0$, and the relative x and y linear acceleration constraints in Eq. (4) simplify to $[a_x \ a_y]_{\text{roll}}^T = \mathbf{0}$.

An expression for the body accelerations of the object ${}^o\dot{\mathcal{V}}_{so}$ as a function of the hand accelerations ${}^h\dot{\mathcal{V}}_{sh}$ and the relative accelerations $\dot{\mathcal{V}}_{\text{rel}}$ is used in the dynamics derivation in Section V. Taking the derivative of Eq. (2) in frame $\{c_h\}$ (following the derivative rule for expressions in different frames from Appendix A-B) gives:

$$\begin{aligned} {}^o\dot{\mathcal{V}}_{so} = & [\text{Ad}_{\mathbf{T}_{oh}}]{}^h\dot{\mathcal{V}}_{sh} + [\text{Ad}_{\mathbf{T}_{och}}]\dot{\mathcal{V}}_{\text{rel}} \\ & + \mathbf{K}_4(\mathbf{q}, \omega_{\text{rel}}, {}^h\omega_{sh}), \end{aligned} \quad (5)$$

where $\mathbf{K}_4(\mathbf{q}, \omega_{\text{rel}}, {}^h\omega_{sh})$ contains the velocity-product terms and is given in Appendix B-C2.

V. ROLLING DYNAMICS

A diagram of the object and hand in rolling contact is shown in Figure 3. The full six-dimensional orientation and position of each body $i \in [o, h]$ is expressed by the transformation matrix $\mathbf{T}_{si} \in SE(3)$ that consists of the rotation matrix $\mathbf{R}_{si} \in SO(3)$ and vector $\mathbf{r}_{si} = (x_{si}, y_{si}, z_{si})$ that give the orientation and position of $\{i\}$ relative to the space frame $\{s\}$. The orientation of each body can be minimally represented by the roll-pitch-yaw Euler angles $\Phi_{si} = (\theta_i, \beta_i, \gamma_i)$. These map to a rotation matrix by combining rotations about the x -, y -, and z -axes of the space frame: $\mathbf{R}_{si}(\Phi_{si}) = \text{Rot}(\mathbf{z}_s, \gamma_i)\text{Rot}(\mathbf{y}_s, \beta_i)\text{Rot}(\mathbf{x}_s, \theta_i)$, where $\text{Rot}(\mathbf{z}_s, \gamma_i)$ is the rotation matrix representing a rotation of angle γ_i about the axis \mathbf{z}_s . The six-dimensional velocity vector for each body is represented by the body twist ${}^i\mathcal{V}_{si} = ({}^i\omega_{si}, {}^i\mathbf{v}_{si})$ expressed in the $\{i\}$ frame for $i \in [o, h]$.

The combined configurations of the object and hand are 12-dimensional, subject to one constraint that the distance between the two bodies is zero. The velocities of the object and hand are 12-dimensional, with three velocity constraints for rolling ($v_x = v_y = v_z = 0$), and four velocity constraints for pure rolling ($v_x = v_y = v_z = \omega_z = 0$). A minimal representation of the state of the system therefore requires 20 states for rolling, or 19 states for pure rolling. The configuration of the hand can be minimally represented by the pair $(\Phi_{sh}, \mathbf{r}_{sh})$, and therefore \mathbf{T}_{so} , the configuration of the object, is fully specified by the hand configuration

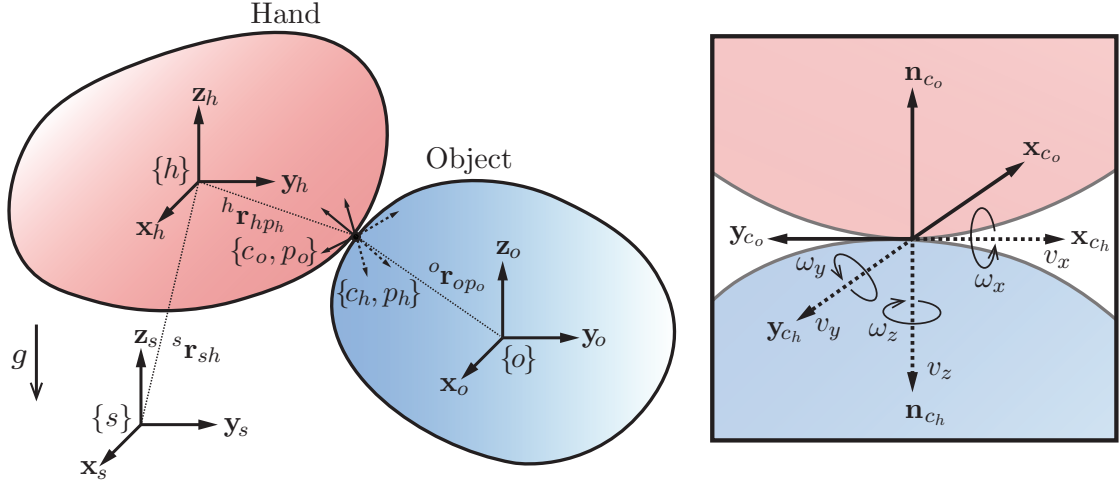


Fig. 3. Rolling rigid bodies in space. The contact coordinate frames $\{c_o, p_o\}$ and $\{c_h, p_h\}$ are shown by solid and dotted coordinate axes respectively. The box shows a zoomed view of the frames at the contact and the relative rotational and linear velocity directions.

$(\Phi_{sh}, \mathbf{r}_{sh})$ and the contact configuration variables \mathbf{q} . The body twist of the hand is represented by ${}^h\mathcal{V}_{sh}$, and the body twist of the object ${}^o\mathcal{V}_{so}$ is fully specified by Eq. (2) using the state of the hand $(\Phi_{sh}, \mathbf{r}_{sh}, {}^h\mathcal{V}_{sh})$, the contact configuration \mathbf{q} , and the relative rolling velocity ω_{rel} . We represent the relative rolling velocity as the five-dimensional vector $\dot{\mathbf{q}}$ from Eq. (1) instead of the three-dimensional ω_{rel} . This adds two variables to the state representation, but allows the evolution of the contact velocities to be integrated using Eq. (3). We therefore define the state of the dynamic rolling system as $\mathbf{s} = (\Phi_{sh}, \mathbf{r}_{sh}, \mathbf{q}, {}^h\mathcal{V}_{sh}, \dot{\mathbf{q}}) \in \mathbb{R}^{22}$ with two constraints on $\dot{\mathbf{q}}$ for rolling and three constraints on $\dot{\mathbf{q}}$ for pure rolling, given in Appendix B-B.

We assume that the hand is directly controlled by acceleration inputs ${}^h\dot{\mathcal{V}}_{sh}$. The model parameters include the contact friction model (rolling vs. pure rolling) and friction coefficient(s), the surface parameterizations $\mathbb{F}_i(\mathbf{u}_i)$, and the spatial inertia matrix of the object, $\mathcal{G}_o = \text{blockdiag}(\mathbf{J}_o, m_o\mathbf{I}_3)$, where \mathbf{J}_o is the rotational inertia matrix for the object, m_o is the mass of the object, and \mathbf{I}_3 is the 3×3 identity matrix. We then solve for dynamic equations describing the motion of the object as follows:

Given:

- 1) Model parameters $\mathbb{F}_i(\mathbf{u}_i)$, \mathcal{G}_o , and friction parameters
- 2) State $\mathbf{s} = (\Phi_{sh}, \mathbf{r}_{sh}, \mathbf{q}, {}^h\mathcal{V}_{sh}, \dot{\mathbf{q}})$
- 3) Acceleration of the hand ${}^h\dot{\mathcal{V}}_{sh} = ({}^h\alpha_{sh}, {}^h\mathbf{a}_{sh})$

find:

- 1) Relative rotational accelerations at the contact α_{rel}
- 2) Contact wrench ${}^{ch}\mathcal{F}_{contact}$

The equations enforce the rolling constraints, so the contact wrench must be examined to see if rolling motion satisfies unidirectional contact constraints and friction limits.

A. Rolling Dynamics Derivation

The six body accelerations of the object ${}^o\dot{\mathcal{V}}_{so}$ are governed by the Newton-Euler equations (see Ch. 8.2 of [34]) and can

be expressed as:

$$\mathcal{G}_o {}^o\dot{\mathcal{V}}_{so} = [\text{ad}_{{}^o\mathcal{V}_{so}}]^\top \mathcal{G}_o {}^o\mathcal{V}_{so} + {}^o\mathcal{F}_{g_o} + {}^o\mathcal{F}_{contact}, \quad (6)$$

where \mathcal{G}_o is the body inertia matrix of the object and ${}^o\mathcal{F}_{g_o}$ is the gravitational wrench on the object. The contact wrench ${}^o\mathcal{F}_{contact}$ is given by ${}^o\mathcal{F}_{contact} = [\text{Ad}_{\mathbf{T}_{c_h o}}]^\top {}^{ch}\mathcal{F}_{contact}$, where ${}^{ch}\mathcal{F}_{contact} = [0 \ 0 \ 0 \ f_x \ f_y \ f_z]^\top$ for rolling and ${}^{ch}\mathcal{F}_{contact} = [0 \ 0 \ \tau_z \ f_x \ f_y \ f_z]^\top$ for pure rolling. Eq. (5) can be substituted into Eq. (6) to obtain:

$$\begin{aligned} [\text{Ad}_{\mathbf{T}_{oc_h}}] \dot{\mathbf{V}}_{rel} - \mathcal{G}_o^{-1} [\text{Ad}_{\mathbf{T}_{c_h o}}]^\top {}^{ch}\mathcal{F}_{contact} = \\ \mathcal{G}_o^{-1} ([\text{ad}_{{}^o\mathcal{V}_{so}}]^\top \mathcal{G}_o {}^o\mathcal{V}_{so} + {}^o\mathcal{F}_{g_o}) \\ - \mathbf{K}_4(\mathbf{q}, \omega_{rel}, {}^h\omega_{sh}) - [\text{Ad}_{\mathbf{T}_{oh}}] {}^h\dot{\mathcal{V}}_{sh}, \end{aligned} \quad (7)$$

where the only unknowns are in $\dot{\mathbf{V}}_{rel}$ and ${}^{ch}\mathcal{F}_{contact}$. We substitute the second-order-rolling constraints $\mathbf{a}_{rel} = \mathbf{a}_{roll}$ in Eq. (4) for rolling, and the additional constraint $\alpha_z = \alpha_{z,pr}$ in Eq. (43) for pure rolling. Rearranging gives us the following forms for rolling and pure rolling, respectively:

$$\mathbf{K}_5(\mathbf{s}) [\alpha_x \ \alpha_y \ \alpha_z \ f_x \ f_y \ f_z]^\top = \mathbf{K}_6(\mathbf{s}) - [\text{Ad}_{\mathbf{T}_{oh}}] {}^h\dot{\mathcal{V}}_{sh}, \quad (8)$$

$$\mathbf{K}_{5_{pr}}(\mathbf{s}) [\alpha_x \ \alpha_y \ \tau_z \ f_x \ f_y \ f_z]^\top = \mathbf{K}_{6_{pr}}(\mathbf{s}) - [\text{Ad}_{\mathbf{T}_{oh}}] {}^h\dot{\mathcal{V}}_{sh}. \quad (9)$$

The expressions for $\mathbf{K}_5(\mathbf{s})$, $\mathbf{K}_6(\mathbf{s})$, $\mathbf{K}_{5_{pr}}(\mathbf{s})$, $\mathbf{K}_{6_{pr}}(\mathbf{s})$ are omitted for brevity, but are the result of straightforward linear algebra on equation (7). An example derivation can be found in the supplemental code. For the rolling assumption, Eq. (8) can be solved to find the relative rotational acceleration at the contact $\alpha_{rel} = [\alpha_x \ \alpha_y \ \alpha_z]^\top$. For the pure-rolling assumption, Eq. (9) can be solved for $[\alpha_x \ \alpha_y]^\top$ and combined with the pure-rolling constraint on α_z from Eq. (43) to construct α_{rel} .

The contact wrenches for rolling and pure rolling can be extracted from Eq. (8) and Eq. (9), respectively:

$${}^{ch}\mathcal{F}_{contact,roll} = [0 \ 0 \ 0 \ f_x \ f_y \ f_z]^\top, \quad (10)$$

$${}^{ch}\mathcal{F}_{contact,pr} = [0 \ 0 \ \tau_z \ f_x \ f_y \ f_z]^\top. \quad (11)$$

For the rolling solution to be valid, the contact wrench must satisfy $f_z \geq 0$ (nonnegative normal force) and $\|(f_x, f_y)\| \leq$

$\mu_s f_z$, where μ_s is the coefficient of static friction. For pure rolling, the contact wrench must also satisfy $\|\tau_z\| \leq \mu_{\text{spin}} f_z$, where μ_{spin} is a torque friction coefficient at the contact. These constraints can be checked in optimization-based motion planning.

B. Simulating the Rolling Dynamics

The state of the dynamic rolling system is defined as $\mathbf{s} = (\Phi_{sh}, \mathbf{r}_{sh}, \mathbf{q}, {}^h\mathcal{V}_{sh}, \dot{\mathbf{q}}) \in \mathbb{R}^{22}$. The state evolution of the hand is directly controlled by the change in body twist ${}^h\dot{\mathcal{V}}_{sh}$. The state of the object is represented by the state of the hand, the contact coordinates \mathbf{q} , and coordinate velocities $\dot{\mathbf{q}}$. The contact coordinate accelerations $\ddot{\mathbf{q}}$ are needed to integrate the contact coordinates over time. An expression for $\ddot{\mathbf{q}}$ is given by the second-order kinematics in Eq. (3), which takes the relative rotational accelerations α_{rel} as an input. The expression for α_{rel} is found by solving Eq. (8) and Eq. (9) for rolling and pure rolling respectively. For both rolling and pure rolling the dynamics equations can be rearranged into the control-affine form

$$\dot{\mathbf{s}} = \mathbf{K}_7(\mathbf{s}) + \mathbf{K}_8(\mathbf{s}) {}^h\dot{\mathcal{V}}_{sh}, \quad (12)$$

where the expressions for $\mathbf{K}_7(\mathbf{s})$ and $\mathbf{K}_8(\mathbf{s})$ are large symbolic expressions that are omitted for brevity (an example derivation can be found in the supplemental code). The evolution of the state \mathbf{s} can be simulated using a numerical integrator such as MATLAB's ode45.

In implementation one can avoid large, symbolic matrix inversions needed to solve for Eq. (12) by numerically evaluating \mathbf{K}_5 and \mathbf{K}_6 from Eq. (8) for rolling or $\mathbf{K}_{5_{\text{pr}}}$ and $\mathbf{K}_{6_{\text{pr}}}$ from Eq. (9) for pure rolling at each time step, solving for α_{rel} , and then solving Eq. (3) numerically for $\ddot{\mathbf{q}}$. The state \mathbf{s} , controls ${}^h\dot{\mathcal{V}}_{sh}$, and $\ddot{\mathbf{q}}$ can then be combined into the vector $\dot{\mathbf{s}}$ from Eq. (12).

C. Example: Ball on a Rotating Plate

To validate our dynamic equations (Eq. (12)) we consider a solid, homogeneous sphere rolling without slipping on a plate spinning at a constant speed about an axis perpendicular to the plate. The plate may be perpendicular to gravity (horizontal) or inclined. This is a well-studied problem (see [33] and Part III.XV of [32]) with analytical solutions for the motion of the sphere. For a horizontal plate, the contact point of the ball rolls in a circular orbit on the plate (Figure 4(a)), and if the plate is inclined in gravity, the motion is the circular orbit plus a constant drift in a direction perpendicular to the gravitational component in the plane of the plate (Figure 4(b)). The circle radius and center point are determined analytically from the initial conditions of the ball. Simulations of the dynamic rolling equations from Section V-B are consistent with the analytical solutions, as demonstrated in the following two examples. MATLAB scripts to simulate these two examples are included in the open-source code.

1) *Horizontal Rotating Plate:* Consider a horizontal plate coincident with the origin of the inertial frame with a constant rotational velocity about its z -axis, ${}^h\omega_{sh,z} = \omega_{\text{plate}}$ (Figure 4(a)). A ball with radius ρ_o is initially in contact with the

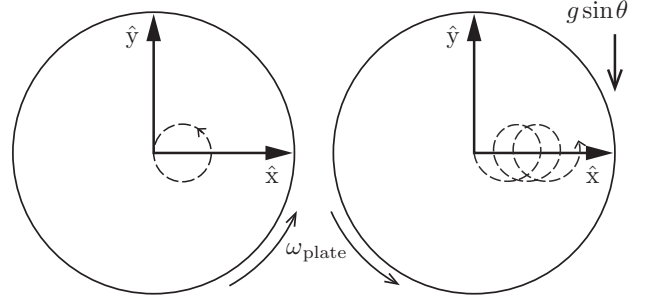


Fig. 4. The x - and y -axes shown are fixed in the inertial frame and aligned with the plate. The plate spins about the z -axis at an angular velocity ω_{plate} . A sphere is initially in contact at the origin and rolling in the $-y$ direction without slipping. (a) The plane of the plate is in the x - y plane of the inertial frame and gravity acts in the $-z$ direction. The contact point of the sphere follows a circular orbit. (b) The plate is tilted by angle θ about the x -axis of the inertial frame, so gravity has a component $g \sin \theta$ in the $-y$ direction. The contact point motion is the sum of the circular orbit and a constant drift in the $+x$ direction.

plate at ${}^h\mathbf{r}_{hc}(0)$, where $\{c_h\}$ is the contact frame on the plate. The ball has an initial linear velocity ${}^h\mathbf{v}_{ho}$ and no rotational velocity. From [33], the ball follows a circular trajectory with the following properties:

$$\omega_c = \frac{2}{7} \omega_{\text{plate}}, \quad (13)$$

$${}^h\mathbf{r}_{hc} = {}^h\mathbf{r}_{hc}(0) - {}^h\mathbf{v}_{ho} \times [0 \ 0 \ 1/\omega_c]^T, \quad (14)$$

$$\rho_c = \|{}^h\mathbf{r}_{hc}(0) - {}^h\mathbf{r}_{hc}\|, \quad (15)$$

where ${}^h\mathbf{r}_{hc}$ and ρ_c are the center and radius of the circle trajectory, respectively, and ω_c is the angular velocity of the contact point about the center of the circle.

For this validation, we choose the following parameters and initial conditions for a ball in contact at the origin that is initially rolling without slipping in the $-y$ direction: $\omega_{\text{plate}} = 7$ rad/s, $\rho_o = 0.2$ m, ${}^h\mathbf{r}_{hc}(0) = [0 \ 0 \ 0]^T$ m, ${}^h\mathbf{v}_{ho} = [0 \ -0.2 \ 0]^T$ m/s. Evaluating at the initial conditions gives $\omega_c = 2$ rad/s, ${}^h\mathbf{r}_{hc} = [0.1 \ 0 \ 0]^T$ m, and $\rho_c = 0.1$ m.

We now simulate the rolling sphere using the dynamic rolling method derived in Section V-A. The surface of the ball is parameterized by the sphere equation $\mathbb{F}_o : \mathbf{u}_o \rightarrow \mathbb{R}^3 : (u_o, v_o) \mapsto (\rho_o \sin(u_o) \cos(v_o), \rho_o \sin(u_o) \sin(v_o), \rho_o \cos(u_o))$, where the “latitude” u_o satisfies $0 < u_o < \pi$. The plate is parameterized as a plane $\mathbb{F}_h : \mathbf{u}_h \rightarrow \mathbb{R}^3 : (u_h, v_h) \mapsto (u_h, v_h, 0)$. The spatial inertia matrix for the sphere is given by $\mathcal{G}_o = \text{blockdiag}(\mathbf{J}_o, m_o \mathbf{I}_3)$, where $\mathbf{J}_o = \frac{2}{5} m_o \rho_o^2 \mathbf{I}_3$, $m_o = 0.1$ kg, and \mathbf{I}_3 is the 3×3 identity matrix. The friction model is rolling (relative spin at the contact allowed), and the static friction μ_s is large enough so slip does not occur.

The state of the sphere-on-plane system can be represented by the state vector $\mathbf{s} = (\Phi_{sh}, \mathbf{r}_{sh}, \mathbf{q}, {}^h\mathcal{V}_{sh}, \dot{\mathbf{q}})$, where $\Phi_{sh}(0) = (0, 0, 0)$, $\mathbf{r}_{sh}(0) = (0, 0, 0)$, $\mathbf{q}(0) = (\pi/2, 0, 0, 0, 0)$, ${}^h\mathcal{V}_{sh}(0) = (0, 0, 7, 0, 0, 0)$, $\omega_{\text{rel}}(0) = (1, 0, -7)$ gives $\dot{\mathbf{q}} = (0, 1, 0, -0.2, -7)$ from Eq. (1), and the control input is given as ${}^h\dot{\mathcal{V}}_{sh}(t) = (0, 0, 0, 0, 0, 0)$.

The first- and second-order kinematic equations for the sphere-on-plane system are found using the expressions in Appendix B. The state of the system is then simulated using the

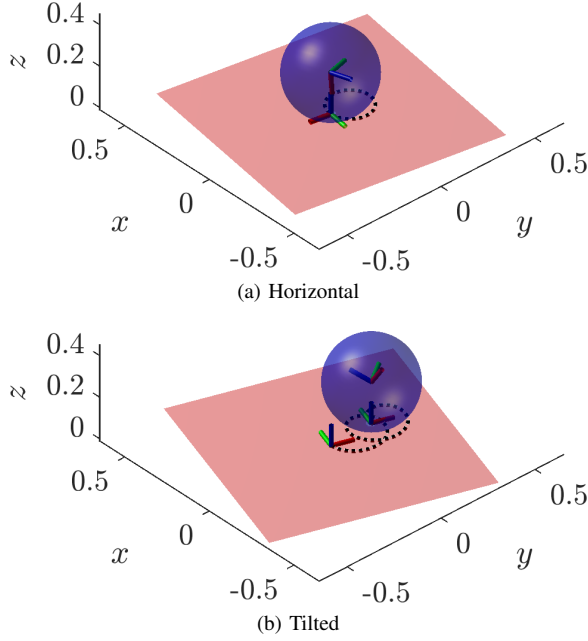


Fig. 5. Visualizations of the sphere-on-plane rolling trajectories for a plane with a constant rotational body velocity ${}^h\omega_{sh,z} = \omega_{\text{plate}} = 7$ rad/s (axis units in meters). The paths are shown by the black, dotted lines for (a) a horizontal plane and (b) a plane tilted by 0.01 rad about the x -axis of the inertial frame (see Figure 4(b)). The spheres move in a counter-clockwise motion along the trajectories with a period of π seconds, and (b) drifts in the x direction at a velocity given by Eq. (16). These results are consistent with the analytical solutions shown in Figure 4 and derived in [33].

kinematics equations and the rolling dynamics in Eq. (12). The simulated rolling trajectory matches the analytical solution by tracing a circular trajectory on the plane of radius $\rho_c = 0.1$ m, centered at ${}^h\mathbf{r}_{hc} = [0.1 \ 0 \ 0]^T$ m, and in $t_f = \pi$ ($\omega_c = 2$ rad/s). A visualization of the trajectory is shown in Figure 5(a), and an animation is included in the supplemental video. We tested the numerical accuracy of our method by simulating the system for 120 seconds with the variable step-size integrator ode45. The divergence of the radius from the analytical circular trajectory was less than $5 \times 10^{-6}\%$, and the average integrator step size was 0.01 seconds.

To compare the accuracy of our approach to a commonly used physics simulator we implemented the rolling example using Bullet Physics C++ version 2.89, and found comparable results except that the object diverged from the circular trajectory over time as shown in Figure 6. Even with a step size of 0.001 seconds this method had much larger errors, and the divergence of the radius from the analytical circular trajectory was 34% after only 10 seconds.

2) *Tilted Rotating Plate*: The motion of a ball on a tilted plate with a constant rotational velocity is a cycloidal orbit with the same rotational velocity ω_c from the previous section but with an additional uniform linear drift velocity perpendicular to the force of gravity given by:

$$v_{\text{drift}} = \frac{5}{2} \frac{g}{\omega_{\text{plate}}} \sin \theta, \quad (16)$$

where g is gravity, $\omega_{\text{plate}} = {}^h\omega_{sh,z}$ is the rotational velocity of the plate about its z -axis and θ is the tilt of the plate creating a gravitational component in the $-y$ direction (see Figure 4(b)).

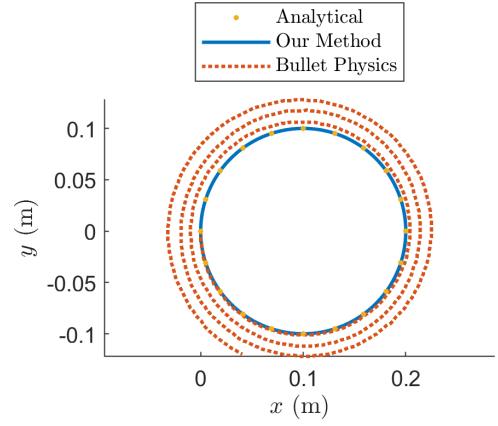


Fig. 6. Comparison of the horizontal rolling trajectory using our method (solid blue) and using the Bullet physics simulator (dashed red) with the same initial conditions and simulated for 10 s. Our method matches the circular analytical trajectory of radius 0.1 m centered at (0.1,0). The Bullet simulation has the same initial conditions but drifts from of the circular trajectory.

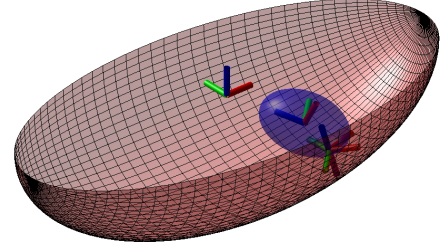


Fig. 7. Dynamic rolling example of an ellipsoid rolling in an ellipsoidal dish. An animation with a pure-rolling friction contact is included in the supplemental video.

We simulate the system for 10 seconds using the same initial conditions and controls for the horizontal case except except with a tilt of 0.01 rad about the x -axis of the inertial frame $\Phi_{sh}(0) = (0.01, 0, 0)$ rad. The sphere follows a circular motion of period π seconds combined with a constant drift velocity of 0.035 m/s which is consistent with Eq. (16). A visualization of the rolling trajectory is shown in Figure 5(b), and an animation is included in the supplemental video.

D. 3D Rolling Example

Our dynamics formulation applies to arbitrary smooth geometries of the object and hand, unlike previous work restricted to specific geometries (e.g., a sphere on a plane) or the rolling contact approximations built into standard physics engines (e.g., Bullet). As one example, Figure 7 illustrates an ellipsoid rolling in an ellipsoidal shaped bowl. An animation with a pure-rolling friction contact is included in the supplemental video, and the derivation is included in the open-source code.

VI. CONTACT JUGGLING MOTION PLANNING

In this section the rolling dynamics equations are used to plan rolling motions that bring the hand and object from an initial state $\mathbf{s}_{\text{start}}$ to a goal state \mathbf{s}_{goal} . This builds on

our previous work in [10] where we demonstrate an iterative planning method for kinematic rolling between smooth objects (the relative rolling velocities are directly controlled). The two primary differences in this implementation are: (1) we replace the kinematic equations of motion with the higher-dimensional dynamic-rolling equations; (2) we incorporate nonlinear constraints to enforce positive normal forces and bounded frictional wrenches.

An “admissible” trajectory is defined as a set of states and controls $\xi(t) = (\mathbf{s}(t), {}^h\dot{\mathbf{v}}_{sh}(t))$, from $t = 0$ to the final time $t = t_f$, that satisfies the rolling dynamics equation (12) and the contact wrench limits. A “valid” trajectory is defined as an admissible trajectory that also satisfies $\mathbf{s}_{\text{error}}(t_f) < \eta$, where η is the tolerance on the final state error and $\mathbf{s}_{\text{error}}(t_f) = \|\mathbf{s}(t_f) - \mathbf{s}_{\text{goal}}\|$, where $\|\cdot\|$ corresponds to a weighted norm that puts state errors in common units. (Throughout the rest of this paper, we use the Euclidean norm.) The motion planning problem can be stated as:

Given: The rolling dynamics equations and contact wrench expressions from Section V, the states $(\mathbf{s}_{\text{start}}, \mathbf{s}_{\text{goal}})$, and the rolling time t_f ,

find: a valid rolling trajectory $\xi(t) = (\mathbf{s}(t), {}^h\dot{\mathbf{v}}_{sh}(t))$ for $t \in [0, t_f]$ that brings the system from $\mathbf{s}(0) = \mathbf{s}_{\text{start}}$ to $\mathbf{s}(t_f) = \mathbf{s}_{\text{goal}}$.

We plan rolling motions by adapting the iterative direct collocation (iDC) nonlinear optimization method described in our recent work [10]. The optimization first solves for a trajectory history that is represented coarsely, using a small number of state and control segments. The solved-for controls are then simulated by a more accurate, higher-order numerical integration method than the integrator implicit in the constraints in the nonlinear optimization. If the simulated trajectory satisfies the error tolerances, the problem is solved. If not, the previous solution is used as an initial guess, the number of state and control segments is increased, and the optimization is called again. This is repeated until a valid trajectory is found, the maximum number of iDC iterations is reached, or the optimization converges to an invalid point. The details are included in Appendix C.

We focus on plans for cases where the object and hand are stationary at $\mathbf{s}_{\text{start}}$. We refer to plans where \mathbf{s}_{goal} is also stationary as “stationary-to-stationary” motions. We refer to plans where \mathbf{s}_{goal} is moving as “stationary-to-rolling” motions, with the special case “stationary-to-freeflight” when the object and hand separate ($f_z = 0, a_{z,\text{rel}} > a_{z,\text{roll}}$) at the final time t_f . The planner can make use of all six hand accelerations ${}^h\dot{\mathbf{v}}_{sh}(t)$, or subsets such as control of the rotational accelerations ${}^h\dot{\boldsymbol{\alpha}}_{sh}$ only or control of the linear accelerations ${}^h\dot{\mathbf{a}}_{sh}$ only.

A. Planning for a Ball on Plate Reconfiguration

Recent work [31] addresses planning and control for dynamic, nonprehensile repositioning and reorientation for a ball on a horizontal plate (the z -axis is aligned with gravity). The ball is initially at rest on the plate, and a goal position and orientation for the ball is given. The controls are the two rotations about the x - and y -axes of the plate. The desired path is

TABLE II
TRAJECTORY OPTIMIZATION PARAMETERS FOR BALL-ON-PLATE
EXAMPLE

Description	Value
Trajectory time t_f	2 s
Initial # of segments N	50 ($\Delta t = 0.04$ s)
Goal error tolerance η	0.1
Max iDC iterations	4
Max fmincon func evals/iter	10^5
Control limits	$\ \alpha_x\ \leq 50, \ \alpha_y\ \leq 50$
Constraint integration method	trapezoidal
Initial guess	stationary
\mathbf{P}_1 (terminal state weight)	$\text{blkdiag}(\mathbf{I}_3, 10\mathbf{I}_2, 1000\mathbf{I}_2, 10, \mathbf{I}_3, 10\mathbf{I}_5)/1000$
\mathbf{Q} (tracking weight)	$\text{blkdiag}(\mathbf{I}_3, 10\mathbf{I}_2, 1000\mathbf{I}_2, 10, \mathbf{I}_3, 10\mathbf{I}_5)/100$
\mathbf{R} (control weight)	$\text{diag}(0.001, 0.001)$

generated by time-scaling a geometric planning method from [25], and then tracked using a feedback controller. An example from the paper is reproduced in Figure 8; The stationary initial and goal configurations for the sphere on the plate are shown in Figure 8(a) and (b), respectively. Visualizations of the contact locations on the hand for the geometric solution are shown by the dashed black lines in Figure 8(c) and (d).

Our method for trajectory planning utilizes the iterative direct collocation method detailed in Appendix C. To match the method above we constrain the hand to have two rotational degrees of freedom. We simplify the dynamics (12) by substituting the constant values $\mathbf{r}_{sh} = {}^h\mathbf{v}_{sh} = {}^h\mathbf{a}_{sh} = \mathbf{0}$, and the constraint on the hand accelerations expressed in the world frame ${}^s\alpha_{sh,z} = 0$. The number of states is therefore decreased from 22 to 16.

We initialize the planner with a stationary trajectory where the ball stays in place and no controls are applied. The iDC algorithm was then run using the parameters given in Table II. The weight \mathbf{Q} was reduced to zero after the first iteration because the inadmissible straight-line trajectory is no longer needed to bias the trajectory towards a solution.

A valid trajectory was found after three iterations of iDC iterative refinement: 50 time segments (planning time 171 s), 100 time segments (346 s), and 200 time segments (946 s), for a total planning time of 24 minutes running on an i7-4700MQ CPU @ 2.40 GHz with 16 GB of RAM. A visualization and plot of the optimized trajectory are shown in Figure 8 (c) and (d) respectively, and an animation is included in the supplemental video. In comparison to the trajectory planner of [31], the optimized plan found by iDC results in a much shorter path length on the hand. An advantage of the planner in [31] is that it returns a plan in negligible time, but the approach applies only to a ball on a plane, whereas the iDC approach with our dynamics formulation applies to general smooth bodies for the hand and object.

VII. FEEDBACK CONTROL FOR DYNAMIC ROLLING

We apply a linear quadratic regulator (LQR) to stabilize the linearized dynamics along a known trajectory [10]. LQR computes a time-varying gain matrix $\mathbf{K}_{\text{LQR}}(t)$ that optimally reduces the total cost for small perturbations about the nominal trajectory. LQR requires a cost function, and we use the one given in Eq. (47), where $\mathbf{s}_{\text{des}}(t)$ is set to the nominal trajectory

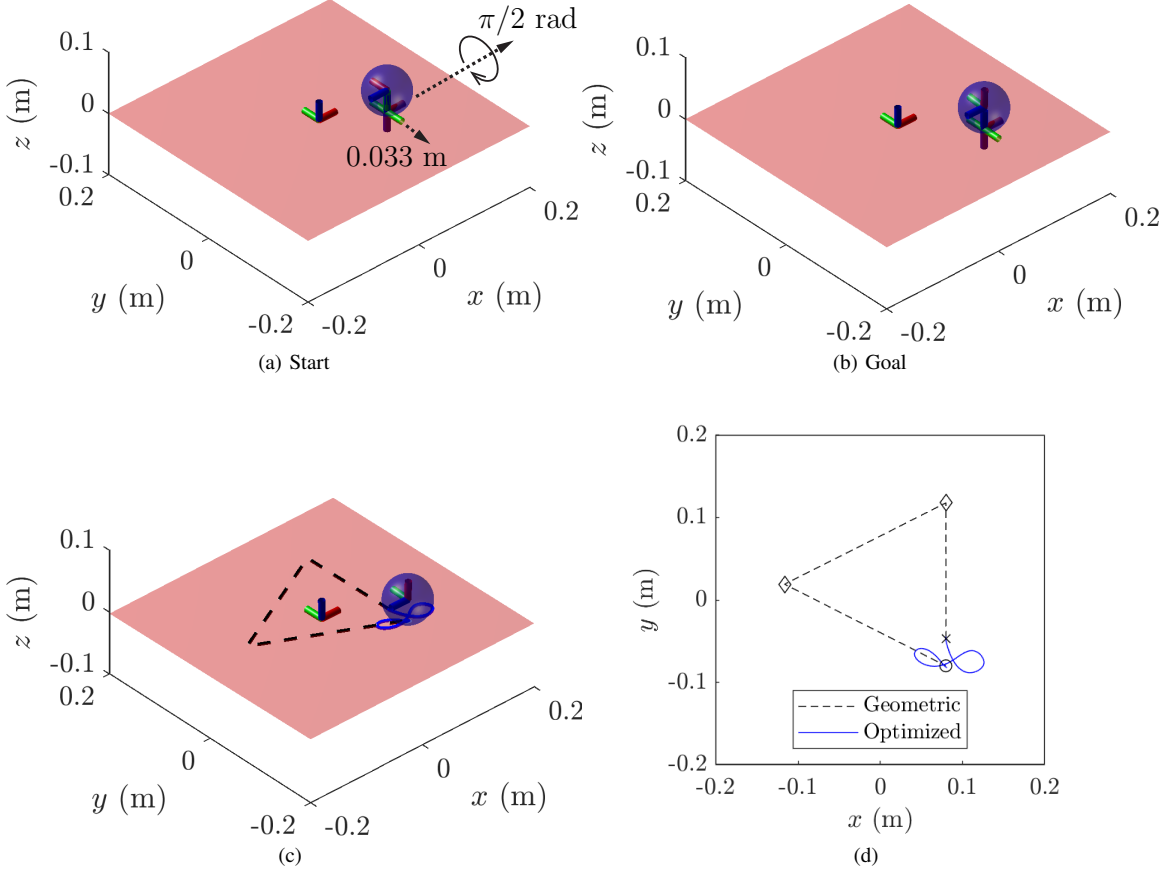


Fig. 8. Initial and goal states for reorienting a sphere on a plate are shown in (a) and (b) respectively. The goal state is 0.033 m from the start state in the $-y$ direction, with the object rotated $\pi/2$ rad about the x -axis. A visualization of the sphere rolling trajectory from the geometric plan from [31] is shown by the black dashed lines in (c) and (d), and the optimized plan from the iterative direct collection method is shown by the solid blue lines. The start position is shown by the “ \times ,” and the goal position is shown by the “ \circ .” An animation of the optimized solution can be seen in the supplemental media.

we are tracking $\mathbf{s}_{\text{nom}}(t)$. We solve the matrix Riccati equation to find the time varying feedback control matrix $\mathbf{K}_{\text{LQR}}(t)$ (see Section 2.3 of [35]).

$$-\dot{\mathbf{P}}(t) = \mathbf{P}(t)\tilde{\mathbf{A}}(t) + \tilde{\mathbf{A}}(t)^\top \mathbf{P}(t) - \mathbf{P}(t)\tilde{\mathbf{B}}(t)\mathbf{R}_{\text{LQR}}^{-1}\tilde{\mathbf{B}}(t)^\top \mathbf{P}(t) + \mathbf{Q}_{\text{LQR}}, \quad (17)$$

$$\mathbf{P}(t_f) = \mathbf{P}_{\text{I,LQR}}$$

$$\mathbf{K}_{\text{LQR}}(t) = \mathbf{R}_{\text{LQR}}^{-1}\tilde{\mathbf{B}}(t)^\top \mathbf{P}(t).$$

The time-varying matrices $\tilde{\mathbf{A}}(t)$ and $\tilde{\mathbf{B}}(t)$ come from linearizing about the nominal trajectory $\mathbf{s}_{\text{nom}}(t)$, and $\mathbf{P}_{\text{I,LQR}}$, \mathbf{Q}_{LQR} , and \mathbf{R}_{LQR} are the controller gain matrices weighting the goal-state error, desired trajectory deviation, and control cost respectively. The time-varying gain matrix $\mathbf{K}_{\text{LQR}}(t)$ from Eq. (17) can be expressed as the function:

$$\mathbf{K}_{\text{LQR}}(t) = \mathcal{K}(\mathbf{s}_{\text{nom}}(t), \mathbf{P}_{\text{I,LQR}}, \mathbf{Q}_{\text{LQR}}, \mathbf{R}_{\text{LQR}}). \quad (18)$$

The matrix $\mathbf{K}_{\text{LQR}}(t)$ is then used in the feedback control law

$${}^h\dot{\mathbf{v}}_{sh,\text{fbk}}(\mathbf{s}, t) = {}^h\dot{\mathbf{v}}_{sh,\text{nom}}(t) - \mathbf{K}_{\text{LQR}}(t)(\mathbf{s}(t) - \mathbf{s}_{\text{nom}}(t)) \quad (19)$$

to stabilize the nominal trajectory. The linearized dynamics are controllable about almost all trajectories (i.e., generic trajectories). Specially chosen trajectories can be uncontrollable, such as those with symmetry properties as demonstrated for kinematic rolling in [10].

A. Feedback Control Example

Consider the optimized open-loop rolling trajectory shown in Fig. 8 (c) and (d). The feedback controller in Eq. (19) provides robustness to (1) initial state error, (2) perturbations along the trajectory, and (3) error due to planning rolling motions using a coarse approximation of the dynamics. In this example we demonstrate how the feedback controller can be used to decrease error from the the third source, the coarse approximation of the dynamics.

As discussed in Section VI, the optimization first solves for a trajectory history that is represented coarsely, using a small number of state and control segments. The solved-for controls are then simulated by a more accurate, higher-order numerical integration method than the integrator implicit in the constraints in the nonlinear optimization. If the final state error in the fine trajectory is too large (i.e., greater than the goal error tolerance η), we perform another iteration of the motion plan with additional state and control segments. The goal error tolerance for this motion plan was given by $\eta = 0.1$ from Table II. To further decrease this error, we stabilize the planned trajectory with a feedback controller.

We generate the time-varying gain matrix $\mathbf{K}_{\text{LQR}}(t)$ by plugging the planned trajectory and gain matrices into Eq. (18), and then stabilize the trajectory using the feedback control

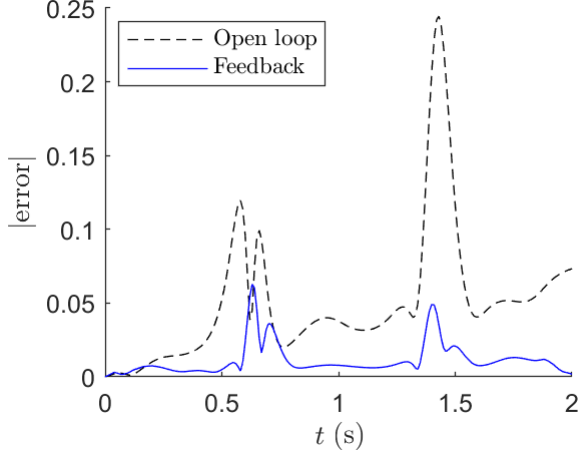


Fig. 9. Comparison of trajectory error over time for open-loop and closed-loop trajectories. The open-loop trajectory uses the coarse set of controls found by the trajectory optimization method which leads to error during the simulation with the finer integration method. Closed-loop control drives the final state to the desired final state. The feedback gains are tuned to eliminate error at the terminal state, which is why some error is not eliminated in the middle of the trajectory. (The two spikes occur where the ball rapidly changes direction, because the coarse dynamics are more sensitive to integration errors at these points.)

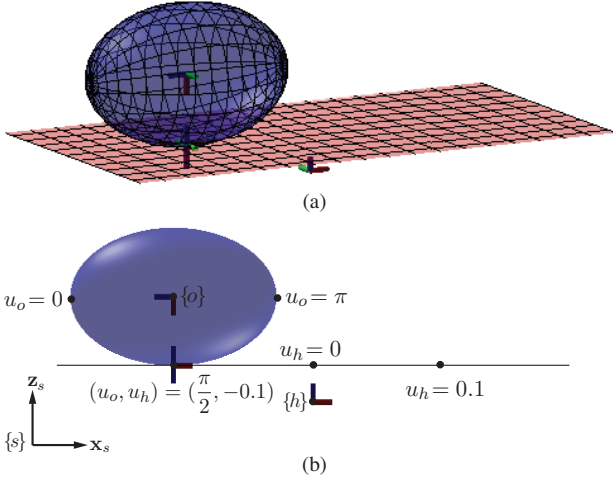


Fig. 10. The full three-dimensional model used for planning rolling motions is shown in (a) and the 2D projection is shown in (b) along with the body frames and some u_o and u_h values.

law from Eq. (19). The open-loop simulation using the higher-order numerical integration method (MATLAB's ode45) gives us the state trajectory $\mathbf{s}_{\text{fine}}(t)$. The closed-loop simulation gives us the state trajectory $\mathbf{s}_{\text{fbk}}(t)$. Plots of the distance errors between the output trajectories and the nominal trajectory $\mathbf{s}_{\text{nom}}(t)$ are shown in Figure 9.

VIII. EXPERIMENTS

This section outlines a series of experiments in planning and feedback control for rolling manipulation tasks. The experiments are in two dimensions, but the model is a full three-dimensional model as shown in Figure 10.

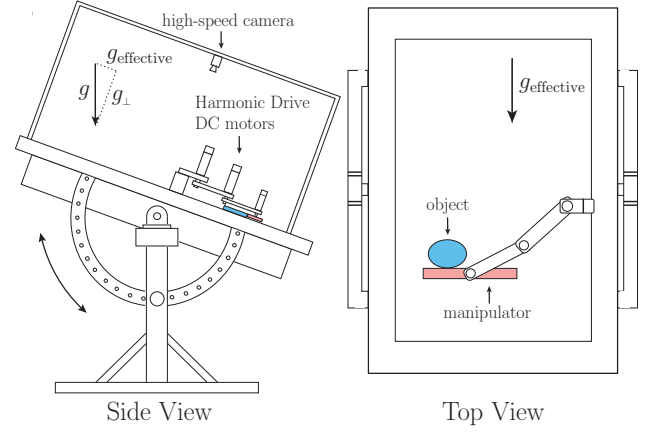


Fig. 11. Diagram of the experimental setup

A. Experimental Setup

The experimental setup consists of a 3-DOF robot arm that moves in a plane parallel to the surface of an inclined air table. A diagram of the experimental setup is shown in Figure 11. Each link is actuated by a brushed DC motor with harmonic drive gearing and current controlled using Junus motor amplifiers. The 1000 Hz motion controller runs on a PC104 embedded computer running the QNX real-time operating system. Vision feedback is given by a 250 Hz IR Optitrack camera and reflective markers attached to the object. The manipulator is a flat plate of width 0.375 m, and the object is an ellipse of mass 0.0553 kg, and major and minor axes given by 0.0754 m and 0.0504 m, respectively. Experiments are conducted at 40% full gravity by inclining the table at 24 degrees with respect to horizontal.

B. 2D Rolling Model

We model the system in full 3D, but restrict object and hand motions to the xz -plane so all the motion is planar as shown in Figure 10(b). All rotations occur about the y -axis, and the full system state $\mathbf{s} = (\Phi_{sh}, \mathbf{r}_{sh}, \mathbf{q}, {}^h\mathcal{V}_{sh}, \dot{\mathbf{q}}) \in \mathbb{R}^{22}$ simplifies to $\mathbf{s}_{2D} = (\beta_{sh}, x_{sh}, z_{sh}, u_o, u_h, {}^h\omega_{sh,y}, {}^h v_{sh,x}, {}^h v_{sh,z}, \dot{u}_o, \dot{u}_h) \in \mathbb{R}^{10}$ and all other states are zero. The controls are also limited to rotational accelerations about the y -axis, and linear accelerations in the xz -plane.

Knowledge of the system states is necessary to run feedback controllers based on our rolling dynamics equations. The six hand states $(\beta_{sh}, x_{sh}, z_{sh}, {}^h\omega_{sh,y}, {}^h v_{sh,x}, {}^h v_{sh,z})$ are estimated using robot encoders, and the object states are estimated using the IR camera that tracks reflective markers on the object. We use the object and hand states to estimate the contact coordinates and velocities on the object and hand $(u_o, u_h, \dot{u}_o, \dot{u}_h)$. We analytically solve for the closest points on the object and plate using equations defining the ellipse and a line.

C. Rolling Damping Controller

The first experiment demonstrates a damping controller that stabilizes an ellipse in rolling contact with a plate in a neighborhood of the stable equilibrium $\mathbf{s}_{2D} =$

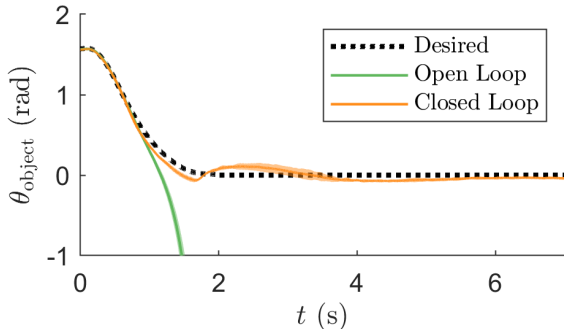


Fig. 12. A plot showing the object angle in the world frame during the flip-up motion. It includes open and closed-loop results, with \pm two standard deviations of the 12 trials shown by the shaded region surrounding the lines. The object overshoot the desired balance state for all of the open-loop trials. All closed-loop trials successfully flipped up the object to the balance position and kept it balanced until shutting off at seven seconds. Snapshots from one trial are shown in Figure 13.

$(0, 0, 0, \pi/2, 0, 0, 0, 0, 0, 0)$. Perturbations of the object cause it to wobble back and forth until dissipation brings it back to rest. We generate the gain matrix \mathbf{K}_{LQR} by plugging the constant nominal trajectory $\mathbf{s}_{2D}(t) = (0, 0, 0, \pi/2, 0, 0, 0, 0, 0, 0)$ and gain matrices into Eq. (18), and stabilize the object using the feedback control law from Eq. (19). When the controller is turned off, the object has large rotational motions in response to perturbations, but the object barely rotates when the controller enabled. The experiment is shown in the supplemental video.

D. Flip Up to Balance

The second experiment is a rolling version of the classic inverted pendulum swing-up to balance problem. We use iDC to plan a flip-up motion and construct an LQR feedback controller to stabilize the trajectory. We also construct a second LQR feedback controller that only stabilizes the goal equilibrium state, and we switch to that controller when the state is in a neighborhood of the goal state.

All of the initial conditions are zero except that $u_o = \pi/2$ and $u_h = -c_{\text{ellipse}}/4$ where c_{ellipse} is the circumference of the ellipse, and the goal states are all zero except $u_o = \pi$. The goal state is at a singularity of the surface parameterization, so we switch to a different coordinate chart to derive the balancing controller.

The contact location and velocity on the object for the planned, open-loop, and closed-loop trajectories are shown in Figure 12. The open-loop execution of the planned trajectories consistently overshoot the goal and the object rolled off the edge of the manipulator. The closed-loop execution was able to stabilize the trajectory and successfully balance the object in 12/12 trials. Snapshots from a successful closed-loop trial are shown in Figure 13, and a video of the 12 closed-loop trials can be seen in the supplemental video.

E. Throw and Catch

We now demonstrate a motion planner for throwing and catching an object in rolling contact with a manipulator. We

found that simple arm trajectories, parameterized by only a few parameters, suffice to achieve most planar throwing goals. To search for optimal parameters in these low-dimensional trajectory spaces, we adopted a shooting method for trajectory optimization rather than iDC.

Our throwing and catching example is inspired by pole throwing, catching, and balancing by quadcopters [36]. The idea is to throw the pole with nonzero angular velocity so that, after a high-friction, inelastic impact with a stationary horizontal surface, the pole has just enough kinetic energy to rotate to the upright position at zero velocity, at which point it can be stabilized in the vertical position.

To plan a throw, catch, and balance of an ellipse, we adapted Eq. (42) from [36] to derive a pre-impact state of the ellipse that, after impact with a stationary horizontal hand, would rotate the ellipse to the vertical position at a desired location. We then used shooting to plan a rolling carry by the hand from an initial rest state to a release state of the ellipse that would carry the ellipse by ballistic free flight to the planned pre-impact state.

For the hand's trajectory, we chose a trapezoidal acceleration profile for the hand's three degrees of freedom, specified by the duration of the carry t_{throw} , the x acceleration of the hand in the body frame $^h a_{sh,x}$, and the rotational acceleration of the hand in the body frame $^h \alpha_{sh,y}$. Note that the hand can still accelerate in the z direction of the $\{s\}$ frame if $\beta_{sh} \neq \{0, \pi\}$. At the release state, the hand accelerates away from the object and moves to its catching position. Because the duration of the throw is short, we performed the throw open-loop. Robustness to small errors in execution comes from the LQR balance controller that turns on after the ellipse impacts the hand.

Snapshots from a throw, catch, and balance are shown in Figure 14, and a trial is shown in the supplemental video.

IX. CONCLUSIONS

This paper demonstrates modeling, motion planning, and feedback control for robotic contact juggling. We first derived the rolling dynamics equations and friction constraints, then validated the results in simulation against known analytical solutions. We used direct collocation methods and the rolling dynamics equations to plan robotic contact juggling motions, and we demonstrated the use of an LQR feedback controller to stabilize planned trajectories in both simulation and experiment.

A. Future Work

There are many possible directions for future work.

1) *Surface Parameterization*: This paper requires orthogonal parameterizations of surfaces, and while any smooth surface can be locally represented this way, deriving orthogonal parameterizations can be cumbersome. We have used non-orthogonal parameterizations for simulating the second-order kinematics by defining local orthogonal frames at each point on the surface, but the dynamics derivation in Section V would need to be modified to relax the orthogonality assumption.

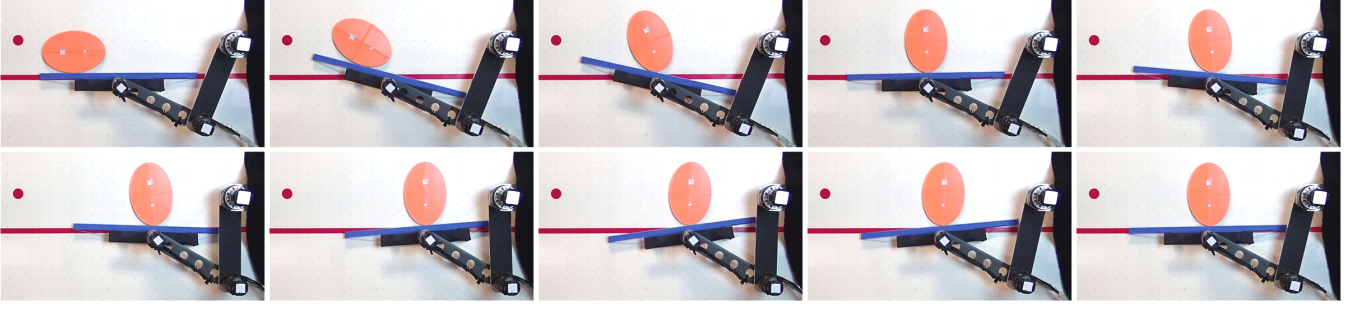


Fig. 13. Demonstration of the closed-loop flip up to balance with LQR stabilization about the trajectory with snapshots taken every 0.5 seconds.

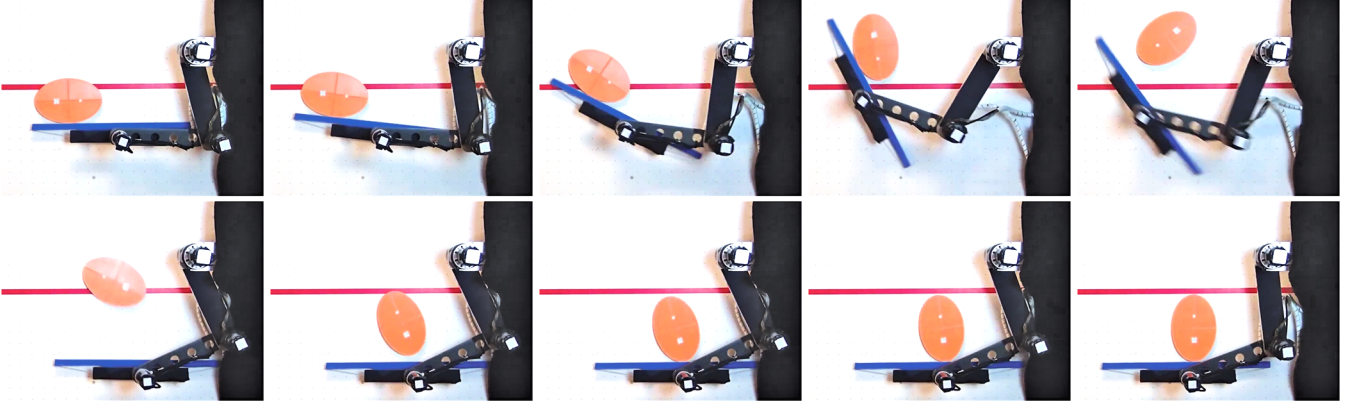


Fig. 14. Snapshots from an experimental rolling throw that flips the object, moves to a catch position where an inelastic, high-friction impact would result in a post-impact velocity that brings the object upright (see [36]), and then balances it about the unstable equilibrium.

Future research could process an object defined by a point-cloud, automatically generate an atlas of coordinate charts that cover the surface, and plan contact juggling with stabilizing feedback controllers through multiple coordinate charts.

2) *Feedback Control*: Our approach to feedback control relies on estimating the contact parameters on the object and hand. In this paper, we rely on vision to estimate the contacts, but tactile sensing could be employed in addition, particularly when coupled with contact state observers [26]. We showed one example of feedback control but there are many areas for extending feedback control for rolling objects. Our method utilizes a linearized LQR controller to stabilize planned trajectories and balance states which results in a simple feedback law given by Eq. (19) that can easily run at high speeds (1000 Hz in our implementation). This method requires knowledge of the contact coordinates which are difficult to estimate for general, 3D rolling motions. Hardware such as manipulators equipped with contact location sensing could help address this, especially if combined with an observability model such as the one developed in [26]. Other feedback methods such as energy-based feedback controllers could be used to stabilize trajectories as well, and may avoid the need for estimating specific contact states [2].

3) *Hybrid Rolling, Sliding, and Free Flight Dynamics*: This paper focuses on rolling and pure rolling, with simple examples of transitions to free flight. Such transitions result in hybrid dynamics. The methods developed in this paper for rolling manipulation can be incorporated in more general

hybrid manipulation planning frameworks, including sliding contacts, such as that described in [37].

APPENDIX A BACKGROUND

A. Operator Definitions

The skew-symmetric matrix form of a vector $\omega = (\omega_x, \omega_y, \omega_z) \in \mathbb{R}^3$ is given by

$$[\omega] = \begin{bmatrix} 0 & -\omega_z & \omega_y \\ \omega_z & 0 & -\omega_x \\ -\omega_y & \omega_x & 0 \end{bmatrix} \in so(3). \quad (20)$$

For a rotation matrix $\mathbf{R} \in SO(3)$, a vector $\mathbf{r} \in \mathbb{R}^3$, and a transformation matrix $\mathbf{T} \in SE(3)$ defined by (\mathbf{R}, \mathbf{r}) , the operator $[\text{Ad}_{\mathbf{T}}]$ is the adjoint map

$$[\text{Ad}_{\mathbf{T}}] = \begin{bmatrix} \mathbf{R} & 0 \\ [\mathbf{r}]\mathbf{R} & \mathbf{R} \end{bmatrix}. \quad (21)$$

For a twist $\mathcal{V} = (\omega, \mathbf{v}) \in \mathbb{R}^6$, the operator $[\text{ad}_{\mathcal{V}}]$ is defined as

$$[\text{ad}_{\mathcal{V}}] = \begin{bmatrix} [\omega] & 0 \\ [\mathbf{v}] & [\omega] \end{bmatrix}, \quad (22)$$

where the Lie bracket of \mathcal{V}_1 and \mathcal{V}_2 is $[\text{ad}_{\mathcal{V}_1}]\mathcal{V}_2$.

B. Derivatives of Expressions in Multiple Frames

The formula for the derivative in frame $\{p_h\}$ of an expression represented in frame $\{o\}$ is

$${}^{p_h}d/dt({}^o\mathbf{v}_{so}) = {}^o\mathbf{a}_{so} + {}^o\omega_{p_h o} \times {}^o\mathbf{v}_{so}. \quad (23)$$

APPENDIX B KINEMATICS EXPRESSIONS

A. Local Geometry of Smooth Bodies

Below are some standard expressions for the geometry of a surface that are used to define the first- and second-order kinematics in the following sections. References and derivations of these expressions can be found in [4].

The surface of each rigid body is represented by an orthogonal parameterization: $\mathbb{F}_i : \mathbf{u}_i \rightarrow \mathbb{R}^3 : (u_i, v_i) \mapsto (x_i, y_i, z_i)$ for $i \in [o, h]$, where the coordinates (x_i, y_i, z_i) are expressed in the $\{i\}$ frame. It is assumed that \mathbb{F}_i is continuous up to the third derivative (class C^3), so that the local contact geometry (contact frames associated with the first derivative of \mathbb{F}_i , curvature associated with the second derivative, and derivative of the curvature associated with the third derivative) are uniquely defined.

The natural bases at a point on a body are given as $\mathbf{x}_{c_i} = \partial \mathbb{F}_i / \partial u_i$ and $\mathbf{y}_{c_i} = \partial \mathbb{F}_i / \partial v_i$. We also assume that coordinate charts are orthogonal ($\mathbf{x}_{c_i} \cdot \mathbf{y}_{c_i} = 0$), and note that \mathbf{x}_{c_i} and \mathbf{y}_{c_i} are not necessarily unit vectors. The unit normal is given as $\mathbf{n}_{c_i} = (\mathbf{x}_{c_i} \times \mathbf{y}_{c_i}) / \|\mathbf{x}_{c_i} \times \mathbf{y}_{c_i}\|$.

The normalized Gauss frame at a point \mathbf{u}_i on body i is defined as the coordinate frame $\{c_i\}$ with origin at $\mathbb{F}_i(\mathbf{u}_i)$ and coordinate axes given by

$$\mathbf{R}_{ic_i} = \left[\frac{\mathbf{x}_{c_i}}{\|\mathbf{x}_{c_i}\|}, \frac{\mathbf{y}_{c_i}}{\|\mathbf{y}_{c_i}\|}, \mathbf{n}_{c_i} \right], \quad (24)$$

where \mathbf{R}_{ic_i} expresses the Gauss frame in the object or hand frame $\{i\}$. The metric tensor \mathbf{G}_i is a 2×2 positive-definite matrix defined as

$$\mathbf{G}_i = \begin{bmatrix} \mathbf{x}_{c_i} \cdot \mathbf{x}_{c_i} & \mathbf{x}_{c_i} \cdot \mathbf{y}_{c_i} \\ \mathbf{y}_{c_i} \cdot \mathbf{x}_{c_i} & \mathbf{y}_{c_i} \cdot \mathbf{y}_{c_i} \end{bmatrix}. \quad (25)$$

The coefficients $g_{jk,i}$ reference the indices of matrix \mathbf{G}_i , and \mathbf{G}_i is diagonal ($g_{12,i} = g_{21,i} = 0$) when the coordinate chart \mathbb{F}_i is orthogonal. The 2×2 matrix \mathbf{L}_i is the second fundamental form given by the expression

$$\mathbf{L}_i = \begin{bmatrix} \frac{\partial^2 \mathbb{F}_i}{\partial u_i^2} \cdot \mathbf{n}_{c_i} & \frac{\partial^2 \mathbb{F}_i}{\partial u_i \partial v_i} \cdot \mathbf{n}_{c_i} \\ \frac{\partial^2 \mathbb{F}_i}{\partial v_i \partial u_i} \cdot \mathbf{n}_{c_i} & \frac{\partial^2 \mathbb{F}_i}{\partial v_i^2} \cdot \mathbf{n}_{c_i} \end{bmatrix}. \quad (26)$$

\mathbf{H}_i combines the metric tensor \mathbf{G}_i with the second fundamental form \mathbf{L}_i and is given by,

$$\mathbf{H}_i = (\sqrt{\mathbf{G}_i})^{-1} \mathbf{L}_i (\sqrt{\mathbf{G}_i})^{-1}. \quad (27)$$

The 1×2 array Γ_i is given by the expression

$$\Gamma_i = [\Gamma_{11,i}^2 \quad \Gamma_{12,i}^2], \quad (28)$$

where $\Gamma_{jk,i}^l$ are Christoffel symbols of the second kind given by

$$\Gamma_{jk,i}^l = \sum_{n=1}^2 \left(\frac{\partial(\chi_i)_j}{\partial(\mathbf{u}_i)_k} \right)^T (\chi_i)_n g_i^{nl}, \quad (29)$$

where $(\chi_i)_j$ is the j^{th} vector in the list $\chi_i = (\mathbf{x}_{c_i}, \mathbf{y}_{c_i})$, $(\mathbf{u}_i)_k$ is the k^{th} variable in the list $\mathbf{u}_i = (u_i, v_i)$, and g_i^{nl} are the

entries (n, l) of the metric tensor inverse $(\mathbf{G}_i)^{-1}$. This gives $\Gamma_{11,i}^2$ and $\Gamma_{12,i}^2$ as

$$\begin{aligned} \Gamma_{11,i}^2 &= \left(\frac{\partial \mathbf{x}_{c_i}}{\partial u_i} \right)^T \mathbf{x}_{c_i} g_i^{12} + \left(\frac{\partial \mathbf{x}_{c_i}}{\partial u_i} \right)^T \mathbf{y}_{c_i} g_i^{22}, \\ \Gamma_{12,i}^2 &= \left(\frac{\partial \mathbf{x}_{c_i}}{\partial v_i} \right)^T \mathbf{x}_{c_i} g_i^{12} + \left(\frac{\partial \mathbf{x}_{c_i}}{\partial v_i} \right)^T \mathbf{y}_{c_i} g_i^{22}. \end{aligned} \quad (30)$$

B. First-Order Kinematics

This form of the first-order kinematics was initially derived in [4]. We reproduce it in matrix form with rolling constraints ($v_x = v_y = v_z = 0$) in Eq. (1) as

$$\dot{\mathbf{q}} = \mathbf{K}_1(\mathbf{q}) \omega_{\text{rel}},$$

with $\omega_{\text{rel}} = {}^{c_h} \omega_{p_h p_o} = [\omega_x \ \omega_y \ \omega_z]^T$ and $\mathbf{K}_1(\mathbf{q})$ defined as:

$$\begin{aligned} \mathbf{K}_1(\mathbf{q}) &= \begin{bmatrix} \mathbf{K}_{1o}(\mathbf{q}) & \mathbf{0}_{2 \times 1} \\ \mathbf{K}_{1h}(\mathbf{q}) & \mathbf{0}_{2 \times 1} \\ \sigma_o \Gamma_o \mathbf{K}_{1o}(\mathbf{q}) + \sigma_h \Gamma_h \mathbf{K}_{1h}(\mathbf{q}) & -1 \end{bmatrix}, \\ \mathbf{K}_{1o}(\mathbf{q}) &= (\sqrt{\mathbf{G}_o})^{-1} \mathbf{R}_\psi (\tilde{\mathbf{H}}_o + \mathbf{H}_h)^{-1} \mathbf{E}_1, \\ \mathbf{K}_{1h}(\mathbf{q}) &= (\sqrt{\mathbf{G}_h})^{-1} (\tilde{\mathbf{H}}_o + \mathbf{H}_h)^{-1} \mathbf{E}_1, \end{aligned} \quad (31)$$

where \mathbf{G}_i is the metric tensor of body $i \in [o, h]$ from Eq. (25), the 2×2 rotation matrix \mathbf{R}_ψ and \mathbf{E}_1 are defined as

$$\mathbf{R}_\psi = \begin{bmatrix} \cos(\psi) & -\sin(\psi) \\ -\sin(\psi) & -\cos(\psi) \end{bmatrix}, \quad \mathbf{E}_1 = \begin{bmatrix} 0 & -1 \\ 1 & 0 \end{bmatrix},$$

\mathbf{H}_i is a 2×2 matrix that gives the curvature of the surface from Eq. (27), $\tilde{\mathbf{H}}_o$ is defined as $\tilde{\mathbf{H}}_o = \mathbf{R}_\psi \mathbf{H}_o \mathbf{R}_\psi$, the scalar σ_i is defined as $\sigma_i = \sqrt{g_{22,i}/g_{11,i}}$ where $g_{11,i}$ and $g_{22,i}$ are the diagonal entries of the metric tensor \mathbf{G}_i , and Γ_i is a 1×2 matrix of the Christoffel symbols of the second kind from Eq. (28).

We use a five-dimensional representation $\dot{\mathbf{q}}$ for the relative rolling velocity at the contact, but these are subject to two constraints for rolling and pure rolling:

$$\mathbf{K}_{1o}(\mathbf{q})^{-1} \dot{\mathbf{u}}_o = \mathbf{K}_{1h}(\mathbf{q})^{-1} \dot{\mathbf{u}}_h. \quad (32)$$

Pure rolling is subject to the constraints above as well as the no-spin constraint $\omega_z = 0$. Eq. (31) gives us:

$$\dot{\psi} = [\sigma_o \Gamma_o \mathbf{K}_{1o}(\mathbf{q}) + \sigma_h \Gamma_h \mathbf{K}_{1h}(\mathbf{q})] \begin{bmatrix} \omega_x \\ \omega_y \end{bmatrix}. \quad (33)$$

C. Second-Order Kinematics

Second-order contact equations were derived by Sarkar et al. in [4] and published again in later works [8], [9]. Errors in the published equations for second-order contact kinematics in [4], [8], [9] were corrected in our recent work [5]. We first define some additional higher-order local contact geometry expressions used in the second-order kinematics first defined in [4], and then provide the corrected second-order-kinematics equations in a newly derived matrix form.

The first order kinematics includes expressions for Γ_i (1×2) and \mathbf{L}_i (2×2). We now give four additional expressions for $\bar{\Gamma}_i$ (2×3), $\bar{\mathbf{L}}_i$ (1×3), $\bar{\Gamma}_i$ (1×3), and $\bar{\mathbf{L}}_i$ (2×3):

$$\bar{\Gamma}_i = \begin{bmatrix} \Gamma_{11,i}^1 & 2\Gamma_{12,i}^1 & \Gamma_{22,i}^1 \\ \Gamma_{11,i}^2 & 2\Gamma_{12,i}^2 & \Gamma_{22,i}^2 \end{bmatrix}, \quad (34)$$

$$\bar{\mathbf{L}}_i = [\mathbf{L}_{11,i} \quad 2\mathbf{L}_{12,i} \quad \mathbf{L}_{22,i}], \quad (35)$$

where $\Gamma_{jk,i}^l$ is the Christoffel symbol of the second kind defined in Eq. (29), and $\mathbf{L}_{jk,i}$ refers to the entry (j, k) of matrix \mathbf{L}_i in Eq. (26). The final two expressions for $\bar{\Gamma}_i$ (1×3) and $\bar{\mathbf{L}}_i$ (2×3) are given as:

$$\bar{\Gamma}_i = \begin{bmatrix} (\Gamma_{21,i}^2 - \Gamma_{11,i}^1)\Gamma_{11,i}^2 + \frac{\partial \Gamma_{11,i}^2}{\partial u_i} \\ (\Gamma_{21,i}^2 - \Gamma_{11,i}^1)\Gamma_{12,i}^2 + (\Gamma_{22,i}^2 - \Gamma_{12,i}^1)\Gamma_{11,i}^2 + \frac{\partial \Gamma_{12,i}^2}{\partial u_i} + \frac{\partial \Gamma_{11,i}^2}{\partial v_i} \\ (\Gamma_{22,i}^2 - \Gamma_{12,i}^1)\Gamma_{12,i}^2 + \frac{\partial \Gamma_{12,i}^2}{\partial v_i} \end{bmatrix}^\top, \quad (36)$$

$$\bar{\mathbf{L}}_i = \begin{bmatrix} \left(\begin{array}{c} \Gamma_{11,i}^1 \mathbf{L}_{11,i} - \frac{\partial \mathbf{L}_{11,i}}{\partial u_i} \\ \Gamma_{11,i}^1 \mathbf{L}_{12,i} + \Gamma_{12,i}^1 \mathbf{L}_{11,i} - \frac{\partial \mathbf{L}_{12,i}}{\partial u_i} - \frac{\partial \mathbf{L}_{11,i}}{\partial v_i} \\ \Gamma_{12,i}^1 \mathbf{L}_{12,i} - \frac{\partial \mathbf{L}_{12,i}}{\partial v_i} \end{array} \right)^\top \\ \left(\begin{array}{c} \Gamma_{21,i}^2 \mathbf{L}_{21,i} - \frac{\partial \mathbf{L}_{21,i}}{\partial u_i} \\ \Gamma_{21,i}^2 \mathbf{L}_{22,i} + \Gamma_{22,i}^2 \mathbf{L}_{21,i} - \frac{\partial \mathbf{L}_{22,i}}{\partial u_i} - \frac{\partial \mathbf{L}_{21,i}}{\partial v_i} \\ \Gamma_{22,i}^2 \mathbf{L}_{22,i} - \frac{\partial \mathbf{L}_{22,i}}{\partial v_i} \end{array} \right)^\top \end{bmatrix}^\top. \quad (37)$$

The second-order kinematics expression can therefore be expressed as:

$$\begin{aligned} \begin{bmatrix} \ddot{\mathbf{u}}_o \\ \ddot{\mathbf{u}}_h \end{bmatrix} &= \begin{bmatrix} \mathbf{R}_\psi \sqrt{\mathbf{G}_o} & -\sqrt{\mathbf{G}_h} \\ \mathbf{R}_\psi \mathbf{E}_1 \mathbf{H}_o \sqrt{\mathbf{G}_o} & -\mathbf{E}_1 \mathbf{H}_h \sqrt{\mathbf{G}_h} \end{bmatrix}^{-1} \\ &\left\{ \begin{bmatrix} -\mathbf{R}_\psi \sqrt{\mathbf{G}_o} \bar{\Gamma}_o \\ \mathbf{R}_\psi \mathbf{E}_1 (\sqrt{\mathbf{G}_o})^{-1} \bar{\mathbf{L}}_o \end{bmatrix} \mathbf{w}_o + \begin{bmatrix} \sqrt{\mathbf{G}_h} \bar{\Gamma}_h \\ -\mathbf{E}_1 (\sqrt{\mathbf{G}_h})^{-1} \bar{\mathbf{L}}_h \end{bmatrix} \mathbf{w}_h \right. \\ &+ \begin{bmatrix} -2\omega_z \mathbf{E}_1 \mathbf{R}_\psi \sqrt{\mathbf{G}_o} & \mathbf{0}_{2 \times 2} \\ -\omega_z \mathbf{R}_\psi \mathbf{H}_o \sqrt{\mathbf{G}_o} & -\dot{\psi} \mathbf{H}_h \sqrt{\mathbf{G}_h} \end{bmatrix} \begin{bmatrix} \dot{\mathbf{u}}_o \\ \dot{\mathbf{u}}_h \end{bmatrix} \\ &\left. - \begin{bmatrix} \mathbf{0}_{2 \times 1} \\ \sigma_o \Gamma_o \dot{\mathbf{u}}_o \begin{bmatrix} \omega_y \\ -\omega_x \end{bmatrix} \end{bmatrix} + \begin{bmatrix} \mathbf{0}_{2 \times 1} \\ \alpha_x \\ \alpha_y \end{bmatrix} - \begin{bmatrix} \mathbf{a}_x \\ \mathbf{a}_y \\ \mathbf{0}_{2 \times 1} \end{bmatrix} \right\}, \\ \ddot{\psi} &= - \begin{bmatrix} \omega_y \\ -\omega_x \end{bmatrix}^\top \mathbf{R}_\psi \mathbf{E}_1 (\sqrt{\mathbf{G}_o})^{-1} \mathbf{L}_o \dot{\mathbf{u}}_o - \alpha_z \\ &+ \sigma_o (\Gamma_o \ddot{\mathbf{u}}_o + \bar{\Gamma}_o \mathbf{w}_o) + \sigma_h (\Gamma_h \ddot{\mathbf{u}}_h + \bar{\Gamma}_h \mathbf{w}_h), \end{aligned} \quad (38)$$

where $\omega_{\text{rel}} = {}^{c_h} \omega_{p_h p_o} = [\omega_x \ \omega_y \ \omega_z]^\top$, $\dot{\omega}_{\text{rel}} = {}^{c_h} \dot{\omega}_{p_h p_o} = [\alpha_x \ \alpha_y \ \alpha_z \ \alpha_x \ \alpha_y \ \alpha_z]^\top$, and \mathbf{w}_i comprises the velocity product terms $[\dot{u}_i^2 \ \dot{u}_i \dot{v}_i \ \dot{v}_i^2]^\top$.

The second-order kinematics expression in Eq. (38) can be expressed in the form of Eq. (3)

$$\ddot{\mathbf{q}} = \mathbf{K}_2(\mathbf{q}, \omega_{\text{rel}}) + \mathbf{K}_3(\mathbf{q}) \dot{\omega}_{\text{rel}},$$

which separates the velocity and acceleration components. The

velocity terms are given by the matrix $\mathbf{K}_2(\mathbf{q}, \omega_{\text{rel}})$ defined as:

$$\begin{aligned} \mathbf{K}_2(\mathbf{q}, \omega_{\text{rel}}) &= \begin{bmatrix} \mathbf{K}_{2a} \\ \mathbf{K}_{2b} \end{bmatrix}, \\ \mathbf{K}_{2a} &= \begin{bmatrix} \mathbf{R}_\psi \sqrt{\mathbf{G}_o} & -\sqrt{\mathbf{G}_h} \\ \mathbf{R}_\psi \mathbf{E}_1 \mathbf{H}_o \sqrt{\mathbf{G}_o} & -\mathbf{E}_1 \mathbf{H}_h \sqrt{\mathbf{G}_h} \end{bmatrix}^{-1} \\ &\left\{ \begin{bmatrix} -\mathbf{R}_\psi \sqrt{\mathbf{G}_o} \bar{\Gamma}_o \\ \mathbf{R}_\psi \mathbf{E}_1 (\sqrt{\mathbf{G}_o})^{-1} \bar{\mathbf{L}}_o \end{bmatrix} \mathbf{w}_o + \begin{bmatrix} \sqrt{\mathbf{G}_h} \bar{\Gamma}_h \\ -\mathbf{E}_1 (\sqrt{\mathbf{G}_h})^{-1} \bar{\mathbf{L}}_h \end{bmatrix} \mathbf{w}_h \right. \\ &+ \begin{bmatrix} -2\omega_z \mathbf{E}_1 \mathbf{R}_\psi \sqrt{\mathbf{G}_o} & \mathbf{0}_{2 \times 2} \\ -\omega_z \mathbf{R}_\psi \mathbf{H}_o \sqrt{\mathbf{G}_o} & -\dot{\psi} \mathbf{H}_h \sqrt{\mathbf{G}_h} \end{bmatrix} \begin{bmatrix} \dot{\mathbf{u}}_o \\ \dot{\mathbf{u}}_h \end{bmatrix} \\ &\left. - \begin{bmatrix} \mathbf{0}_{2 \times 1} \\ \sigma_o \Gamma_o \dot{\mathbf{u}}_o \begin{bmatrix} \omega_y \\ -\omega_x \end{bmatrix} \end{bmatrix} \right\}, \\ \mathbf{K}_{2b} &= - \begin{bmatrix} \omega_y \\ -\omega_x \end{bmatrix}^\top \mathbf{R}_\psi \mathbf{E}_1 (\sqrt{\mathbf{G}_o})^{-1} \mathbf{L}_o \dot{\mathbf{u}}_o \\ &+ \sigma_o \bar{\Gamma}_o \mathbf{w}_o + \sigma_h \bar{\Gamma}_h \mathbf{w}_h + [\sigma_o \Gamma_o \quad \sigma_h \Gamma_h] \mathbf{K}_{2a}. \end{aligned} \quad (39)$$

The matrix that operates on the acceleration terms of the second-order kinematics is given by $\mathbf{K}_3(\mathbf{q})$:

$$\mathbf{K}_3(\mathbf{q}) = \begin{bmatrix} \mathbf{I}_{4 \times 4} & \mathbf{0}_{4 \times 1} \\ [\sigma_o \Gamma_o \quad \sigma_h \Gamma_h] & -1 \end{bmatrix} \mathbf{K}_{3a}(\mathbf{q}), \quad (40)$$

where

$$\mathbf{K}_{3a}(\mathbf{q}) = \begin{bmatrix} \begin{bmatrix} \mathbf{R}_\psi \sqrt{\mathbf{G}_o} & -\sqrt{\mathbf{G}_h} \\ \mathbf{R}_\psi \mathbf{E}_1 \mathbf{H}_o \sqrt{\mathbf{G}_o} & -\mathbf{E}_1 \mathbf{H}_h \sqrt{\mathbf{G}_h} \end{bmatrix}^{-1} & \mathbf{0}_{4 \times 1} \\ \mathbf{0}_{1 \times 4} & 1 \end{bmatrix} \mathbf{E}_2,$$

$$\mathbf{E}_2 = \begin{bmatrix} 0 & 0 & 0 & -1 & 0 & 0 \\ 0 & 0 & 0 & 0 & -1 & 0 \\ 1 & 0 & 0 & 0 & 0 & 0 \\ 0 & 1 & 0 & 0 & 0 & 0 \\ 0 & 0 & 1 & 0 & 0 & 0 \end{bmatrix}.$$

1) Second-Order Rolling and Pure Rolling Constraints:

The relative linear accelerations $\mathbf{a}_{\text{rel}} = {}^{c_h} \mathbf{a}_{p_h p_o}$ are constrained by the second-order rolling constraints $\mathbf{a}_{\text{rel}} = \mathbf{a}_{\text{roll}}$. These were derived in Eq. (60) of [4]. The general version is given in Eq. (4) and the full form is reproduced below:

$$\mathbf{a}_{\text{roll}} = \begin{bmatrix} a_x \\ a_y \\ a_z \end{bmatrix}_{\text{roll}} = \begin{bmatrix} -\omega_z \mathbf{E}_1 \\ \omega_y \\ -\omega_x \end{bmatrix}^\top \mathbf{R}_\psi \sqrt{\mathbf{G}_o} \dot{\mathbf{u}}_o. \quad (41)$$

The relative rotational acceleration α_z is constrained by the second-order-pure-rolling constraints $\alpha_z = \alpha_{z,\text{pr}}$. This was given in [4] as $\alpha_{z,\text{pr}} = 0$. We found this to be valid for simple geometries such as sphere-on-sphere, sphere-on-plane, and ellipsoid-on-plane, but for more complex geometries such as ellipsoid-on-ellipsoid and sphere-on-ellipsoid, $\alpha_{z,\text{pr}} = 0$ did not enforce the no-spin constraint.

To derive the rolling constraint we set the derivative of the expression for ω_z from the first-order kinematics equal to zero:

$$\frac{d}{dt} \omega_z = \frac{d}{dt} (\sigma_o \Gamma_o \dot{\mathbf{u}}_o + \sigma_h \Gamma_h \dot{\mathbf{u}}_h - \dot{\psi}) = 0. \quad (42)$$

From Eq. (42) and the second-order kinematics in Eq. (39) we solved for an expression of the form:

$$\alpha_{z,\text{pr}} = d_1(\mathbf{q}, \omega_{\text{rel}}) + d_2(\mathbf{q}) \begin{bmatrix} \alpha_x \\ \alpha_y \end{bmatrix}. \quad (43)$$

For the ellipsoid-on-ellipsoid, and ellipsoid-on-sphere models we tested, Eq. (43) simplified to:

$$\alpha_{z,\text{pr}} = (\omega_{\text{rel}} \times {}^{c_h}\omega_{oc_o})^\top \mathbf{n}_h, \quad (44)$$

where \mathbf{n}_h is the unit contact normal of $\{c_h\}$. This expression is equivalent to the following term from the $\ddot{\psi}$ expression in the second-order kinematics in Eq (38):

$$\alpha_{z,\text{pr}} = - \begin{bmatrix} \omega_y \\ -\omega_x \end{bmatrix}^\top \mathbf{R}_\psi \mathbf{E}_1 (\sqrt{\mathbf{G}_o})^{-1} \mathbf{L}_o \dot{\mathbf{u}}_o. \quad (45)$$

2) *Relative Acceleration Expression:* Eq. (5) gives an expression for the body acceleration of the object given the body acceleration of the hand and the relative acceleration at the contact, and is reproduced below:

$$\begin{aligned} {}^o\dot{\mathbf{v}}_{so} &= [\text{Ad}_{\mathbf{T}_{oh}}] {}^h\dot{\mathbf{v}}_{sh} + [\text{Ad}_{\mathbf{T}_{oc_h}}] \dot{\mathbf{v}}_{\text{rel}} \\ &\quad + \mathbf{K}_4(\mathbf{q}, \omega_{\text{rel}}, {}^h\omega_{sh}). \end{aligned}$$

The velocity product terms \mathbf{K}_4 are given by:

$$\begin{aligned} \mathbf{K}_4(\mathbf{q}, \omega_{\text{rel}}, {}^h\omega_{sh}) &= [\text{Ad}_{\mathbf{T}_{oh}}] \begin{bmatrix} \mathbf{0}_{3 \times 1} \\ [{}^h\omega_{sh}]([{}^h\omega_{sh}] {}^h\mathbf{r}_{hp_h}) \end{bmatrix} \\ &\quad - [\text{Ad}_{\mathbf{T}_{oc_h}}] \begin{bmatrix} [\omega_{\text{rel}}](\mathbf{R}_{c_h o} {}^o\omega_{so}) \\ \mathbf{0}_{3 \times 1} \end{bmatrix} \\ &\quad - \begin{bmatrix} \mathbf{0}_{3 \times 1} \\ [{}^o\omega_{so}]([{}^o\omega_{so}] {}^o\mathbf{r}_{op_o}) \end{bmatrix}, \end{aligned} \quad (46)$$

where ${}^o\omega_{so}$ comes from Eq (2), and the $[\text{Ad}_{\mathbf{T}}]$, \mathbf{r} , and \mathbf{R} expressions can be derived from the contact configuration \mathbf{q} .

APPENDIX C

ITERATIVE DIRECT COLLOCATION

We first describe the details of the direct collocation method, and then outline our iterative version. Direct collocation is a method for trajectory optimization that optimizes an objective function $\mathcal{J}(\xi(t)) = \mathcal{J}(\mathbf{s}(t), {}^h\dot{\mathbf{v}}_{sh}(t))$ using polynomial spline approximations of the continuous states and controls. We chose to use trapezoidal collocation where the control trajectory ${}^h\dot{\mathbf{v}}_{sh}(t)$ is represented by piecewise-linear splines, the state trajectory $\mathbf{s}(t)$ is represented by quadratic splines, and the trapezoidal rule is used for integration. Higher-order representations such as Hermite-Simpson collocation can also be used but with increased computational cost [38]. We define the objective function $\mathcal{J}(\mathbf{s}(t), {}^h\dot{\mathbf{v}}_{sh}(t))$ as the sum of the terminal cost and the running cost and omit the dependence on t for clarity:

$$\begin{aligned} \mathcal{J}(\mathbf{s}, {}^h\dot{\mathbf{v}}_{sh}) &= \mathcal{M}(\mathbf{s}(t_f)) + \int_0^{t_f} \mathcal{L}(\mathbf{s}, {}^h\dot{\mathbf{v}}_{sh}) dt, \\ \mathcal{M}(\mathbf{s}(t_f)) &= \frac{1}{2}(\mathbf{s}(t_f) - \mathbf{s}_{\text{goal}})^\top \mathbf{P}_1 (\mathbf{s}(t_f) - \mathbf{s}_{\text{goal}}), \\ \mathcal{L}(\mathbf{s}, {}^h\dot{\mathbf{v}}_{sh}) &= \frac{1}{2}(\mathbf{s} - \mathbf{s}_{\text{des}})^\top \mathbf{Q} (\mathbf{s} - \mathbf{s}_{\text{des}}) + \frac{1}{2} {}^h\dot{\mathbf{v}}_{sh}^\top \mathbf{R} {}^h\dot{\mathbf{v}}_{sh}, \end{aligned} \quad (47)$$

where \mathbf{P}_1 , \mathbf{Q} , and \mathbf{R} , penalize goal-state error, desired trajectory deviation, and control cost respectively, and $\mathbf{s}_{\text{des}}(t)$ is a desired trajectory. The path $\mathbf{s}_{\text{des}}(t)$ is chosen as the linear interpolation from $\mathbf{s}_{\text{start}}$ to \mathbf{s}_{goal} , which penalizes motions that do not move \mathbf{s} towards the goal. Note that $\mathbf{s}_{\text{des}}(t)$ is not admissible in general (i.e., the states and controls do not satisfy the rolling dynamics equations).

The collocation method divides the trajectory $\xi(t)$ into N segments, and the $N+1$ nodes at the ends of each segment are called collocation points. Each collocation point is expressed as $\xi_k(t) = (\mathbf{s}(t_k), {}^h\dot{\mathbf{v}}_{sh}(t_k))$ for $k \in [0, \dots, N]$. For systems with m state variables and n control variables there are a total of $(N+1)(m+n)$ collocation points. The dynamics between each pair of sequential collocation points are enforced by the following condition:

$$\begin{aligned} \mathbf{s}_{k+1} - \mathbf{s}_k &= \frac{1}{2} \Delta t_k (\mathcal{F}(\mathbf{s}_{k+1}, {}^h\dot{\mathbf{v}}_{sh,k+1}) + \mathcal{F}(\mathbf{s}_k, {}^h\dot{\mathbf{v}}_{sh,k})), \\ k &\in [0, \dots, N-1], \end{aligned} \quad (48)$$

where $\Delta t_k = (t_{k+1} - t_k)$ indicates the interval duration and $\mathcal{F}(\mathbf{s}, {}^h\dot{\mathbf{v}}_{sh}) = \mathbf{K}_7(\mathbf{s}) + \mathbf{K}_8(\mathbf{s}) {}^h\dot{\mathbf{v}}_{sh}$ is the rolling dynamics function from Eq. (12). Equation (48) is unique to the choice of trapezoidal collocation, and other integration methods require a different constraint [38].

The optimal control problem can be represented as the following nonlinear programming problem:

$$\begin{aligned} \arg \min_{\mathbf{s}(t_k), {}^h\dot{\mathbf{v}}_{sh}(t_k)} \quad & \mathcal{M}(\mathbf{s}(t_f)) + \sum_{i=0}^N \mathcal{L}(\mathbf{s}(t_i), {}^h\dot{\mathbf{v}}_{sh}(t_i)) \Delta t_i \\ \text{such that} \quad & \mathcal{H}(\mathbf{s}(t_0) : \mathbf{s}(t_N); {}^h\dot{\mathbf{v}}_{sh}(t_0) : {}^h\dot{\mathbf{v}}_{sh}(t_{N-1})) = 0, \\ & \mathcal{I}(\mathbf{s}(t_0) : \mathbf{s}(t_N); {}^h\dot{\mathbf{v}}_{sh}(t_0) : {}^h\dot{\mathbf{v}}_{sh}(t_{N-1})) \leq 0, \end{aligned} \quad (49)$$

where $\mathcal{H}(\cdot)$ enforces the rolling dynamics in Eq. (48), and gives the equality constraints $\mathbf{s}(0) = \mathbf{s}_{\text{start}}$ (and optionally $\mathbf{s}(t_f) = \mathbf{s}_{\text{goal}}$ which can be relaxed by replacing with a high weighting matrix on the goal state \mathbf{P}_1). The expression $\mathcal{I}(\cdot)$ includes the contact wrench inequality constraints on Eq. (10), the controls limits (${}^h\dot{\mathbf{v}}_{sh,\text{min}} \leq {}^h\dot{\mathbf{v}}_{sh} \leq {}^h\dot{\mathbf{v}}_{sh,\text{max}}$), and enforces any constraints on the configurations (e.g., due to singularities in the coordinate chart). Equation (49) is a finite-dimensional nonlinear optimization problem, and a solution $\xi_{\text{iDC}}(t)$ can be found using nonlinear optimizers such as SNOPT, IPOPT, or MATLAB's `fmincon`.

The integration error can be determined by comparing the trajectory $\mathbf{s}_{\text{iDC}}(t)$ from the direct collocation method with the trajectory $\mathbf{s}_{\text{fine}}(t)$, where $\mathbf{s}_{\text{fine}}(t)$ is obtained by integrating the initial state over the interval $t = [0, t_f]$ using Eq. (12), the piecewise-linear output controls ${}^h\dot{\mathbf{v}}_{sh,\text{iDC}}(t)$, and a higher-order integrator with small time steps (e.g. $dt \leq 0.001$). With fewer segments N , the integration error is larger, but there are fewer constraints for the nonlinear solver. This means that the optimizer is more likely to find a solution, and with less computational cost. The choice of N is therefore a trade-off between computational cost/optimizer convergence and integration error. We implemented the iterative direct collocation (iDC) method to address this.

We first run the nonlinear optimization method using MATLAB's `fmincon` for a small number of segments (e.g. $N = 25$) to find a trajectory $\xi_{\text{IDC}}(t)$. The recalculated path $s_{\text{fine}}(t)$ is found using smaller integration timesteps and a higher-order integrator (`ode45`), and the planner is terminated if the goal-state tolerance of the fine trajectory is satisfied ($s_{\text{error}}(t_f) < \eta$). If the goal-state error is too large, the previous output trajectory serves as the initial trajectory guess for the next iteration with twice as many segments ($N \rightarrow 2N$) (N could also be increased by a fixed value ΔN between each iteration to add an additional tuning parameter for the planning method). This is repeated until a valid trajectory $\xi_{\text{sol}}(t)$ is found, the maximum number of IDC iterations is reached, or the optimization converges to an invalid point.

In our tests, an initial optimization with a fine control discretization often takes an unnecessarily long time to converge or even fails to converge to a feasible solution. The coarse initial guess followed by successive refinement yields higher-quality solutions faster and more consistently. The iterative refinement process acts as a form of regularization.

Additional methods can improve the planning success such as ignoring the friction inequality constraints for the initial iteration(s), and decreasing/zeroing the weight Q that penalizes trajectories that do not track a straight line to the goal state.

ACKNOWLEDGMENT

We would like to thank Paul Umbanhowar and Shufeng Ren for helpful discussions while developing this work.

REFERENCES

- [1] K. M. Lynch, N. Shiroma, H. Arai, and K. Tanie, "The roles of shape and motion in dynamic manipulation: the butterfly example," in *Proceedings. 1998 IEEE International Conference on Robotics and Automation*, vol. 3, 1998, pp. 1958–1963 vol.3.
- [2] M. Cefalo, L. Lanari, and G. Oriolo, "Energy-based control of the butterfly robot," *IFAC Proceedings Volumes*, vol. 39, no. 15, 2006.
- [3] M. Surov, A. Shiriaev, L. Freidovich, S. Gusev, and L. Paramonov, "Case study in non-prehensile manipulation: planning and orbital stabilization of one-directional rollings for the "butterfly" robot," in *2015 IEEE International Conference on Robotics and Automation (ICRA)*. IEEE, 2015, pp. 1484–1489.
- [4] N. Sarkar, V. Kumar, and X. Yun, "Velocity and acceleration analysis of contact between three-dimensional rigid bodies," *Journal of Applied Mechanics*, vol. 63, no. 4, pp. 974–984, 1996.
- [5] J. Z. Woodruff and K. M. Lynch, "Second-order contact kinematics between three-dimensional rigid bodies," *Journal of Applied Mechanics*, vol. 86, no. 8, May 2019.
- [6] D. J. Montana, "The kinematics of contact and grasp," *The International Journal of Robotics Research*, vol. 7, no. 3, pp. 17–32, 1988.
- [7] K. Harada, T. Kawashima, and M. Kaneko, "Rolling based manipulation under neighborhood equilibrium," *The International Journal of Robotics Research*, vol. 21, no. 5-6, pp. 463–474, 2002.
- [8] N. Sarkar, X. Yun, and V. Kumar, "Dynamic control of 3-D rolling contacts in two-arm manipulation," *IEEE Transactions on Robotics and Automation*, vol. 13, no. 3, pp. 364–376, Jun. 1997.
- [9] N. Sarkar, Xiaoping Yun, and V. Kumar, "Control of contact interactions with acatastatic nonholonomic constraints," *The International Journal of Robotics Research*, vol. 16, no. 3, pp. 357–374, Jun. 1997.
- [10] J. Z. Woodruff, S. Ren, and K. M. Lynch, "Motion planning and feedback control of rolling bodies," *IEEE Access*, vol. 8, pp. 31 780–31 791, 2020.
- [11] M. Xiao and Y. Ding, "Contact kinematics between three-dimensional rigid bodies with general surface parameterization," *Journal of Mechanisms and Robotics*, vol. 13, no. 2, 2021.
- [12] O. Taylor and A. Rodriguez, "Optimal shape and motion planning for dynamic planar manipulation," *Autonomous Robots*, vol. 43, no. 2, pp. 327–344, 2019.
- [13] J.-C. Ryu and K. M. Lynch, "Contact juggling of a disk with a disk-shaped manipulator," *IEEE Access*, vol. 6, pp. 60 286–60 293, 2018.
- [14] S. R. Erumalla, S. Pasupuleti, and J.-C. Ryu, "Throwing, catching, and balancing of a disk with a disk-shaped end effector on a two-link manipulator," *Journal of Mechanisms and Robotics*, vol. 10, no. 5, 2018.
- [15] V. Lippiello, F. Ruggiero, and B. Siciliano, "The effect of shapes in input-state linearization for stabilization of nonprehensile planar rolling dynamic manipulation," *IEEE Robotics and Automation Letters*, vol. 1, no. 1, pp. 492–499, 2016.
- [16] D. Serra, F. Ruggiero, A. Donaire, L. R. Buonocore, V. Lippiello, and B. Siciliano, "Control of nonprehensile planar rolling manipulation: A passivity-based approach," *IEEE Transactions on Robotics*, vol. 35, no. 2, pp. 317–329, 2019.
- [17] M. Anitescu, J. F. Cremer, and F. A. Potra, "Formulating three-dimensional contact dynamics problems," *Journal of Structural Mechanics*, vol. 24, no. 4, pp. 405–437, 1996.
- [18] T. Liu and M. Y. Wang, "Computation of three-dimensional rigid-body dynamics with multiple unilateral contacts using time-stepping and gauss-seidel methods," *IEEE Transactions on Automation Science and Engineering*, vol. 2, no. 1, pp. 19–31, 2005.
- [19] V. Duindam and S. Stramigioli, "Modeling the kinematics and dynamics of compliant contact," in *2003 IEEE International Conference on Robotics and Automation*, vol. 3. IEEE, 2003, pp. 4029–4034.
- [20] S. Ivaldi, J. Peters, V. Padois, and F. Nori, "Tools for simulating humanoid robot dynamics: a survey based on user feedback," in *IEEE-RAS International Conference on Humanoid Robots*. IEEE, 2014, pp. 842–849.
- [21] V. Jurdjevic, "The geometry of the plate-ball problem," *Archive for Rational Mechanics and Analysis*, vol. 124, no. 4, pp. 305–328, 1993.
- [22] D. Hristu-Varsakelis, "The dynamics of a forced sphere-plate mechanical system," *IEEE Transactions on Automatic Control*, vol. 46, no. 5, pp. 678–686, 2001.
- [23] H. Date, M. Sampei, M. Ishikawa, and M. Koga, "Simultaneous control of position and orientation for ball-plate manipulation problem based on time-state control form," *IEEE transactions on robotics and automation*, vol. 20, no. 3, pp. 465–480, 2004.
- [24] G. Oriolo and M. Vendittelli, "A framework for the stabilization of general nonholonomic systems with an application to the plate-ball mechanism," *IEEE Transactions on Robotics*, vol. 21, no. 2, pp. 162–175, 2005.
- [25] A. Becker and T. Bretl, "Approximate steering of a plate-ball system under bounded model perturbation using ensemble control," in *2012 IEEE/RSJ International Conference on Intelligent Robots and Systems*. IEEE, 2012, pp. 5353–5359.
- [26] Y.-B. Jia and M. Erdmann, "Local observability of rolling," in *Workshop on Algorithmic Foundation of Robotics*, 1998, pp. 251–263.
- [27] P. Choudhury and K. M. Lynch, "Rolling manipulation with a single control," *The International Journal of Robotics Research*, vol. 21, no. 5-6, pp. 475–487, 2002.
- [28] R. Gahleitner, "Ball on ball: Modeling and control of a novel experiment set-up," *IFAC-PapersOnLine*, vol. 48, no. 1, pp. 796–801, 2015.
- [29] K.-K. Lee, G. Batz, and D. Wollherr, "Basketball robot: Ball-on-plate with pure haptic information," in *2008 IEEE International Conference on Robotics and Automation*. IEEE, 2008, pp. 2410–2415.
- [30] G. Bätz, A. Yaqub, H. Wu, K. Kühnlenz, D. Wollherr, and M. Buss, "Dynamic manipulation: Nonprehensile ball catching," in *18th Mediterranean Conference on Control and Automation, MED'10*. IEEE, 2010, pp. 365–370.
- [31] D. Serra, J. Ferguson, F. Ruggiero, A. Siniscalco, A. Petit, V. Lippiello, and B. Siciliano, "On the experiments about the nonprehensile reconfiguration of a rolling sphere on a plate," in *2018 26th Mediterranean Conference on Control and Automation (MED)*. IEEE, 2018, pp. 13–20.
- [32] E. A. Milne, *Vectorial mechanics*. Methuen & Company, 1957.
- [33] K. Weltner, "Stable circular orbits of freely moving balls on rotating discs," *American Journal of Physics*, vol. 47, no. 11, pp. 984–986, 1979.
- [34] K. M. Lynch and F. C. Park, *Modern robotics: mechanics, planning, and control*. Cambridge University Press, 2017.
- [35] B. D. Anderson and J. B. Moore, *Optimal control: linear quadratic methods*. Courier Corporation, 2007.
- [36] D. Bresciani, M. Hehn, and R. D'Andrea, "Quadrocopter pole acrobatics," in *2013 IEEE/RSJ International Conference on Intelligent Robots and Systems*. IEEE, 2013, pp. 3472–3479.
- [37] J. Z. Woodruff and K. M. Lynch, "Planning and control for dynamic, nonprehensile, and hybrid manipulation tasks," in *IEEE International Conference on Robotics and Automation*. IEEE, 2017, pp. 4066–4073.
- [38] M. Kelly, "An introduction to trajectory optimization: How to do your own direct collocation," *SIAM Review*, vol. 59, no. 4, pp. 849–904, 2017.